RESEARCH ARTICLE

Impact of the Madden–Julian Oscillation on extreme precipitation over the western Maritime Continent and Southeast Asia

Nicolas A. Da Silva[1] | Adrian J. Matthews[2]

[1]Centre for Ocean and Atmospheric Sciences, School of Environmental Sciences, University of East Anglia, Norwich, UK

[2]Centre for Ocean and Atmospheric Sciences, School of Environmental Sciences and School of Mathematics, University of East Anglia, Norwich, UK

Correspondence
A. Matthews, School of Environmental Sciences, University of East Anglia, Norwich, NR4 7TJ, UK
Email: a.j.matthews@uea.ac.uk

Abstract

The western Maritime Continent (MC) and Southeast Asia lie at the heart of the largest area of high precipitation on Earth. Extreme precipitation is one of the major high-impact weather events to affect the population of over 500 million in this region. The deep convection associated with this extreme precipitation is difficult to forecast, even with modern high-resolution numerical weather prediction with explicit convection. However, larger-scale organised convective systems, such as the Madden–Julian Oscillation (MJO), can be skilfully predicted to 3–5 weeks lead time. The MJO has a well-known precipitation signal, and it is likely that it also modulates extreme precipitation. Here, the extreme precipitation signal of the MJO is analysed in detail for the western MC and Southeast Asia using 19 years of high-resolution Integrated Multi-satellitE Retrievals for Global Precipitation Measurement (GPM IMERG) data. The probability of experiencing extreme precipitation increases robustly by a factor of two, and decreases by a factor of half, dependent on location and the phase of the MJO. The spatial pattern of these changes in extreme precipitation does not describe a smooth eastward propagation, but shows rapid variation over short distances, tied to the complex distribution of land and sea within the archipelago. There is also a seasonal dependence of this MJO modulation in some locations. A more detailed analysis of the effect of the MJO on extreme precipitation is presented for the major cities in the region. Extreme precipitation days over the MC are generally linked with an amplification of the diurnal cycle. However, although an active MJO increases the frequency of extreme precipitation days and therefore an amplified diurnal cycle, there was no further amplification of the diurnal cycle in the active MJO, compared with extreme precipitation days during non-active MJO periods.

KEYWORDS
extreme precipitation, extreme rainfall, high-impact weather, MC, MJO, precipitation probability

1 | INTRODUCTION

Extreme precipitation is one of the main forms of high-impact weather (HIW) events in the MC. Extreme precipitation is closely associated with devastating floods (Rodysill *et al.*, 2019), which are frequent in the MC and have major societal impacts (Adhikari *et al.*, 2010). In Indonesia, 30% of natural disasters were associated with flooding events (Dewata and Umar, 2019). These events are all the more devastating in the MC because the population in these countries is particularly vulnerable (Hijioka *et al.*, 2014).

In recent decades, the frequency and the intensity of extreme rainfall have increased in the MC (Endo *et al.*, 2009), and a further increase is projected in the future in the context of global climate change (Mandapaka and Lo, 2018). Precipitation in the MC also varies strongly on other time scales: interannual (Juneng and Tangang, 2005; Zhang *et al.*, 2016), interseasonal (Meehl, 1987; Kang *et al.*, 2019), intraseasonal (Peatman *et al.*, 2014; Xavier *et al.*, 2014) and diurnal (Love *et al.*, 2011; Peatman *et al.*, 2014; Birch *et al.*, 2016). Accurate predictions of extreme precipitation in the MC are therefore crucial and can limit the impact of such events. However, state-of-the-art weather prediction models struggle to forecast precipitation correctly in this region, partially as a result of complex interactions between topography and different scales of motion (Chang *et al.*, 2005; Qian, 2008; Birch *et al.*, 2016).

The MJO (Xie *et al.*, 1963; Madden and Julian 1971) is a large-scale weather system that crosses the tropical Indian Ocean, MC and Pacific Ocean from west to east within approximately 30–60 days. During boreal summer, it develops a northward component of propagation in addition to the eastward component (Yasunari, 1979; Krishnamurti and Subrahmanyam, 1982), and is often known as the Boreal Summer Intraseasonal Oscillation (BSISO; Jiang *et al.*, 2004) during this season. The MJO cycle is conveniently divided into eight phases using the real-time multivariate MJO (RMM) index of Wheeler and Hendon (2004). An alternative eight-phase representation is provided by the univariate outgoing long-wave radiation (OLR)-based MJO index (OMI), which is based solely on the convective signal of the MJO (Kiladis *et al.*, 2014). The MJO has been identified as the main source of predictability in the tropics and can be skilfully predicted 3–5 weeks ahead by global weather forecasting models (Kim *et al.*, 2018; Wang *et al.*, 2019). Since the MJO has a major impact on mean and extreme precipitation in the MC (Matthews *et al.*, 2013; Peatman *et al.*, 2014; Xavier *et al.*, 2014), better characterization of this impact could improve the predictability of HIW in the MC.

Xavier *et al.* (2014) used Tropical Rainfall Measuring Mission (TRMM) satellite-derived precipitation (Kummerow *et al.*, 2000), the APHRODITE gridded rain gauge dataset (Yatagai *et al.*, 2012) and local rain gauge data from Singapore to evaluate the impact of the MJO on precipitation extremes in the MC. They found that extreme precipitation over the equatorial (averaged from 10° S to 10° N) land and sea areas of the MC was strongly enhanced during the active period of the MJO (averaged over RMM phases 2–4 in this region), while also concluding that precipitation extremes in certain regions such as north-west Borneo, eastern Malaysia and north-east Borneo did not appear to be related to the MJO.

The objective of this paper is to build on previous studies to further quantify the impact of the MJO on precipitation extremes over the western MC. We take advantage of the longer time series (nearly 20 years) of high-resolution satellite precipitation data that are now available. This allows us to investigate the effect of the MJO on extreme precipitation with finer time discrimination (using the eight individual MJO phases) and finer spatial discrimination (at the grid point scale). These are key components as the MJO precipitation cycle is known to vary significantly in its timing and strength over relatively small spatial scales (Peatman *et al.*, 2014). The general characteristics of the MJO are known to vary strongly with season (Zhang and Dong, 2004), with topography (Matthews *et al.*, 2013) and between land and sea (Peatman *et al.*, 2014; Birch *et al.*, 2016), and the effects of these on extreme precipitation are examined. We also investigate the role of the diurnal cycle in extreme precipitation and the MJO. Finally, this study aims to provide an estimation of the confidence of change of precipitation extremes due to the MJO in the MC.

Section 2 describes the datasets used in this study. Preliminary analysis of the climatological mean precipitation and extreme precipitation distributions are presented in Section 3. The main analysis of the impact of the MJO on extreme precipitation is presented in Section 4, an analysis of the diurnal cycle of extreme precipitation and its modulation by the MJO is provided in Section 5 and conclusions are drawn in Section 6.

2 | DATA

The analysis is based on the Integrated Multi-Satellite Retrievals (IMERG) product, version V06B, from the Global Precipitation Measurement (GPM) project (Huffman *et al.*, 2019). This product is based on measurements from a constellation of satellites, equipped with passive microwave (PM) and geo-infrared (IR) sensors. The PM measurements give more accurate, direct estimations of precipitation rate but have limited spatial and temporal coverage. Meanwhile, the IR measurements only measure

precipitation indirectly, but have almost complete spatial and temporal coverage.

Among PM satellites, the GPM core observatory is considered to carry the most advanced instruments for precipitation detection (Skofronick-Jackson *et al.*, 2018). It was launched in February 2014 and is the successor to the TRMM satellite (Huffman *et al.*, 2007). As well as providing accurate precipitation measurements for the IMERG product, the TRMM satellite and the GPM core observatory serve for inter-calibration of the whole IMERG PM satellite constellation, in their respective eras.

Prior to inter-calibration, the TRMM and GPM core observatory estimates are seasonally corrected over land areas by the Global Precipitation Climatology Project (GPCP) satellite-gauge product (Adler *et al.*, 2018). The IR data, which essentially measure cloud-top features rather than precipitation directly, are trained and calibrated against the PM estimates using an artificial neural network cloud classification system (PERSIANN-CSS; Nguyen *et al.*, 2018).

All precipitation estimates are gridded on to a 0.1° × 0.1° longitude–latitude spatial grid. A Kalman smoother is then used to combine all the precipitation estimates into a single half-hourly estimate (Joyce and Xie, 2011). In this, the IR estimates are incorporated into a Kalman filter in the form of an observation correcting the PM 'forecast'.

The resulting half-hourly estimates over land are then multiplied by the ratio between the GPCP monthly gauge estimate with the monthly sum of half-hourly estimates derived in the early steps of the IMERG algorithm. The IMERG product is thus a multi satellite-gauge precipitation dataset for which data are provided with a 30-min time interval on a global 0.1° × 0.1° grid.

Many studies have identified improvements of precipitation estimates by IMERG relative to its predecessors TRMM and PERSIANN in Southeast Asia (Prakash *et al.*, 2016; Kim *et al.*, 2017; Tan and Santo, 2018; Xu *et al.*, 2019). To our knowledge, IMERG has not yet been compared with the Climate Prediction Center MORPHing (CMORPH, Joyce *et al.*, 2004) dataset in the MC. Studies of IMERG and CMORPH in other regions show no clear evidence that one systematically outperforms the other in detecting extreme precipitation (Wei *et al.*, 2018; Lee *et al.*, 2019; Alsumaiti *et al.*, 2020; Xiao *et al.*, 2020). A recent study using nearly 20 years of gauge precipitation from Singapore, and taking into account their spatial sampling error, found that IMERG accurately represents extreme precipitation in this region (Mandapaka and Lo, 2020). Fang *et al.* (2019) concluded that IMERG captures well the overall spatial patterns and probabilities of extreme rainfall over China, despite potentially under- or overestimating extreme precipitation, which makes it useful for studying the climatology of extreme rainfall, as in the present study.
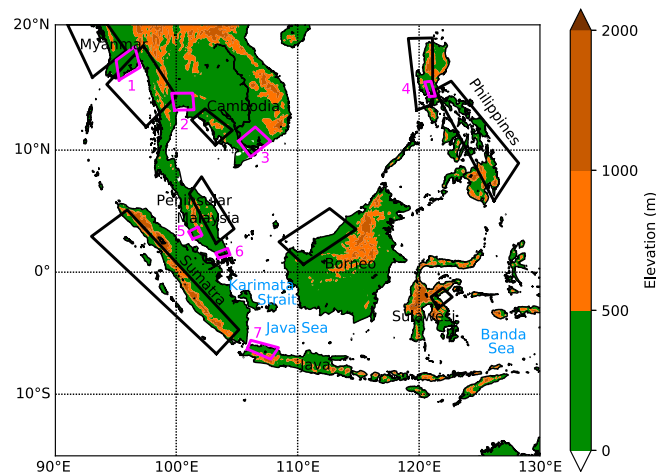

FIGURE 1 Topography of the western MC. Black boxes correspond to the nine selected high-precipitation areas, and magenta boxes correspond to the seven selected high-population areas, which are used for the analysis in Sections 4.4 and 4.5 (respectively). The magenta numbers refer to cities: Yangon (1), Bangkok (2), Ho Chi Minh City (3), Manila (4), Kuala Lumpur (5), Singapore (6) and Jakarta (7) [Colour figure can be viewed at wileyonlinelibrary.com]

Here, we use the IMERG precipitation dataset from January 1, 2001 until December 31, 2019 over the western MC (90–130° E, 20° S to 20° N). Daily mean values were first calculated from the 30-min IMERG data.

A topography dataset was used to distinguish between sea, lowland and mountain regions. The General Bathymetric Chart of the Oceans (GEBCO) topography dataset was regridded from its 30 arc-second native resolution to the coarser 0.1° × 0.1° longitude–latitude IMERG grid (Figure 1).

3 | CLIMATOLOGICAL DISTRIBUTION OF MEAN AND EXTREME PRECIPITATION

The annual mean precipitation over the western MC is above 5 mm·day⁻¹ over most of the domain, with large areas receiving over 10 mm·day⁻¹ on average (Figure 2a). The spatial distribution of mean precipitation is heterogeneous, with notable maxima over the coast of Myanmar, the equatorial eastern Indian Ocean and the west coast of Sumatra, north-west and central Borneo, and the eastern Philippines and western Pacific along 10° N. This precipitation distribution is consistent with earlier studies using the TRMM product (As-syakur *et al.*, 2016; Hassim and Timbal, 2019), to which GPM IMERG is a direct successor.

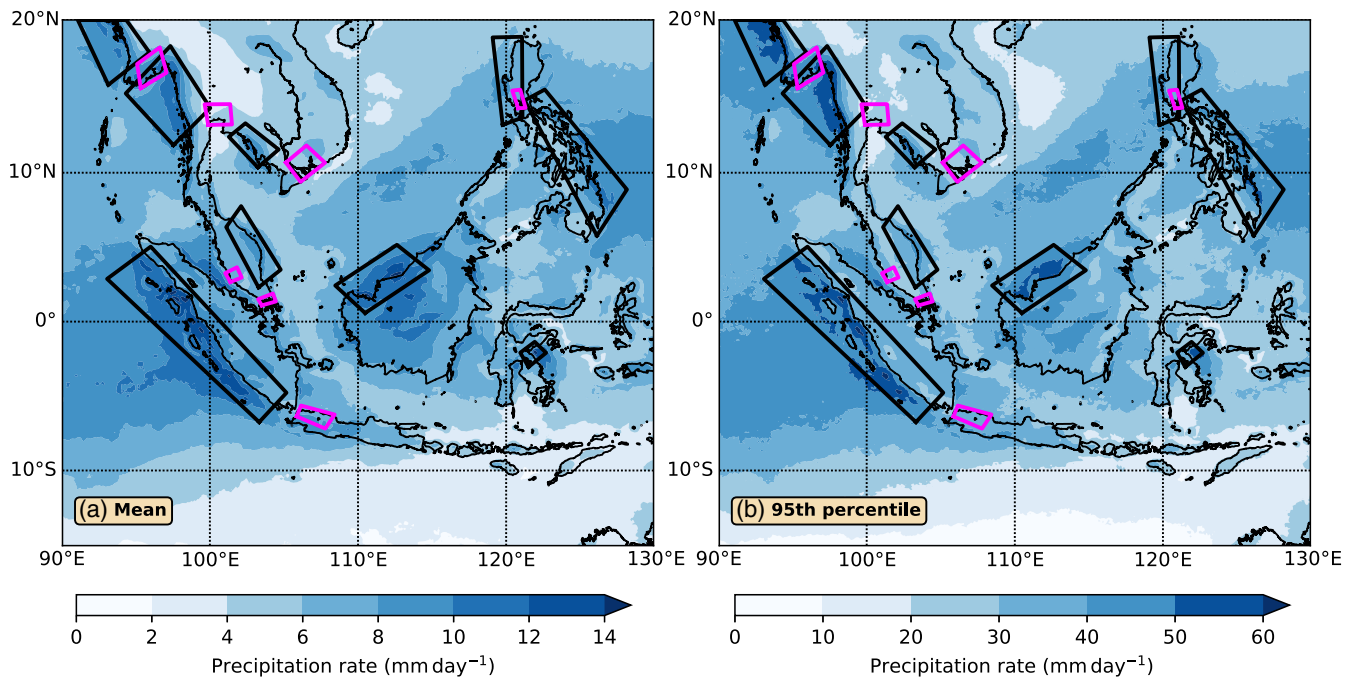A map of the median precipitation (i.e. the 50th percentile of daily mean precipitation rate; not shown) shows

FIGURE 2   Distribution of (a) mean precipitation rate and (b) 95th percentile of daily mean precipitation rate, over the western MC from IMERG, for the period from January 1, 2001 to December 31, 2019. The black and magenta boxes are as in Figure 1 [Colour figure can be viewed at wileyonlinelibrary.com]

reduced values (not exceeding 8 mm·day^{-1}) when compared with the mean, indicating that the distribution of daily rainfall is positively skewed, with a relatively small number of high-precipitation days having a large impact on the mean.

Extreme rainfall on a given day was defined to have occurred if two criteria were satisfied, where the daily mean precipitation rate must exceed: (a) a fixed percentile (95th or 99th) of the distribution of daily mean precipitation rate at that grid point, and (b) an absolute threshold of 20 mm·day^{-1}. Note that, in locations where the fixed percentile exceeds the absolute threshold of 20 mm·day^{-1}, the second criterion is redundant. In locations where the fixed percentile is below the absolute threshold, the first criterion is redundant.

The spatial distribution of the 95th percentile (Figure 2b) is similar to that of the mean (Figure 2b), with the coastal areas of northern Myanmar, southern Myanmar, western Cambodia, eastern Peninsular Malaysia, north-western Philippines, eastern Philippines, western Sumatra, north-west Borneo and eastern Sulawesi in particular being regions of high extreme precipitation. These regions are denoted by black boxes in Figures 1 and 2a,b, and are analysed in greater detail in Section 4.4.

Separate analyses (not shown) of the distribution of extreme rainfall over the western MC for boreal winter (October–March) and summer (April–September) emphasise seasonal features, consistent with the migration of the

Asian–Australian monsoon system northwards in boreal summer and southwards in boreal winter. These include seasonal maxima over Myanmar (Htway and Matsumoto, 2011), Cambodia and the north-western Philippines during boreal summer, and the eastern coast of Peninsular Malaysia, and the eastern Philippines during boreal winter (Tangang *et al.*, 2017; Basconcillo *et al.*, 2016).

The 95th percentile of grid point daily precipitation (Figure 2b) falls below 20 mm·day^{-1} in the southern regions of the domain south of 10° S, reflecting the relatively low mean precipitation in this region (Figure 2a). Such a low value cannot be considered as extreme precipitation, hence the addition of the second criterion of an absolute threshold. The highest 95th percentile values in the study region exceed 50 mm·day^{-1} over: western Myanmar, western Sumatra, western Borneo and the eastern Philippines. Therefore, precipitation extremes, as defined in our study, range from relatively modest events to genuinely high-impact events.

The choice of a higher percentile of daily precipitation rate would have retained only the most extreme daily precipitation events. To this end, the analysis was repeated using the 99th percentile, giving qualitatively similar results to the analysis using the 95th percentile. However, due to the much smaller sample size of extreme events using the higher threshold, the results were less robust, and the main results are presented using the 95th percentile.
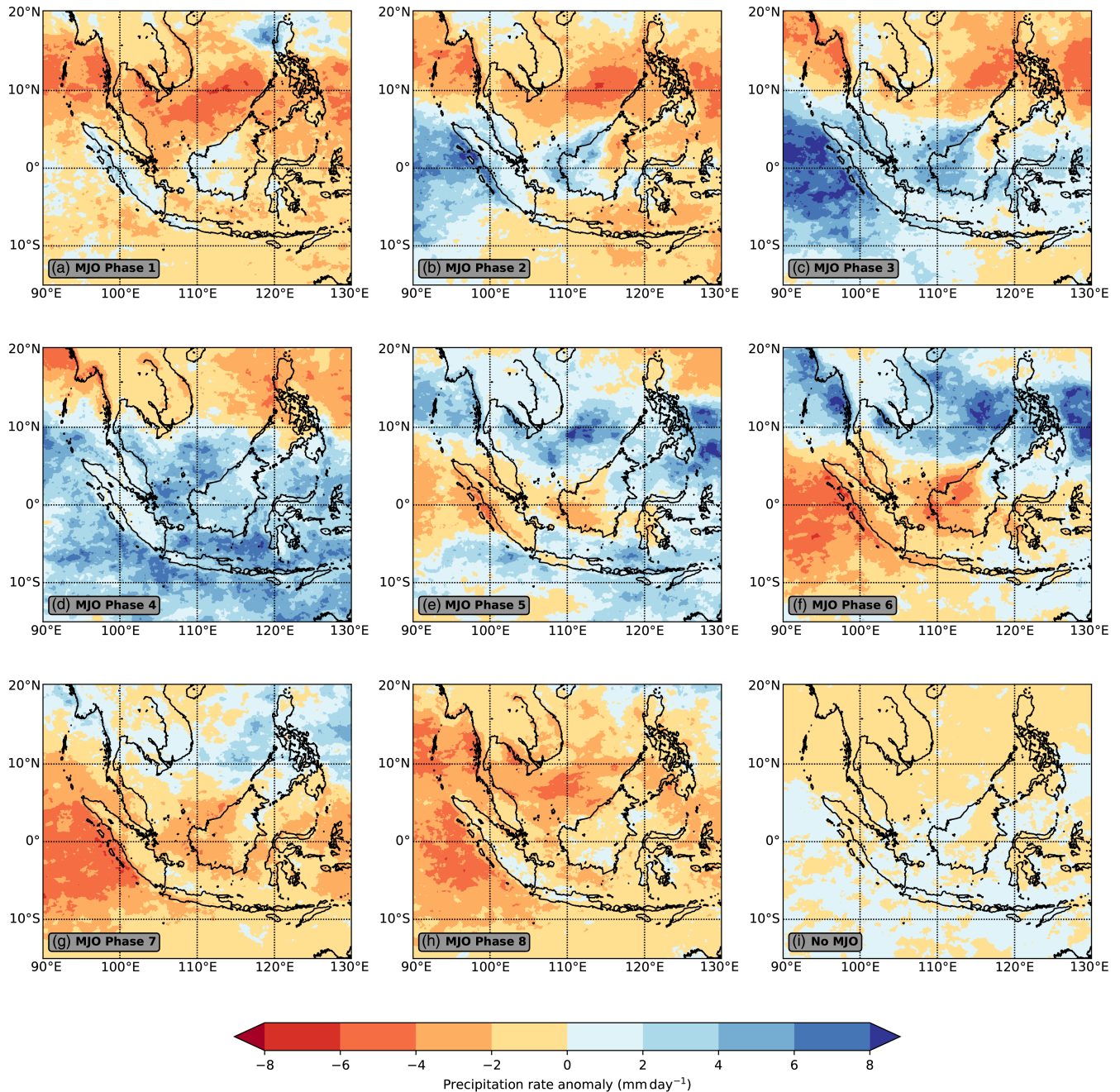
FIGURE 3 Precipitation rate anomaly over the western MC for: MJO phase (a) 1, (b) 2, (c) 3, (d) 4, (e) 5, (f) 6, (g) 7 and (h) 8, and (i) no MJO [Colour figure can be viewed at wileyonlinelibrary.com]

4 | IMPACT OF MJO ON EXTREME PRECIPITATION

4.1 | Standard MJO cycle of precipitation

The MJO makes a large contribution to the intraseasonal variability of precipitation in the MC, as shown by Figure 3, which presents mean precipitation anomalies computed for each of the standard eight MJO phases using the OMI (Kiladis *et al.*, 2014). In MJO phase 1 (Figure 3a), the main envelope of enhanced MJO precipitation (positive anomalies) is over the western Indian Ocean, outside of the domain in the figure here. The majority of the MC experiences suppressed precipitation (negative anomalies). However, a 'vanguard' of precipitation has advanced ahead of the main area, over western Sumatra and western Borneo, as noted by Peatman *et al.* (2014).

During phase 2 (Figure 3b), the main envelope progresses eastward and poleward, such that by phases 3 and 4 (Figure 3c,d) it covers the western MC, and all
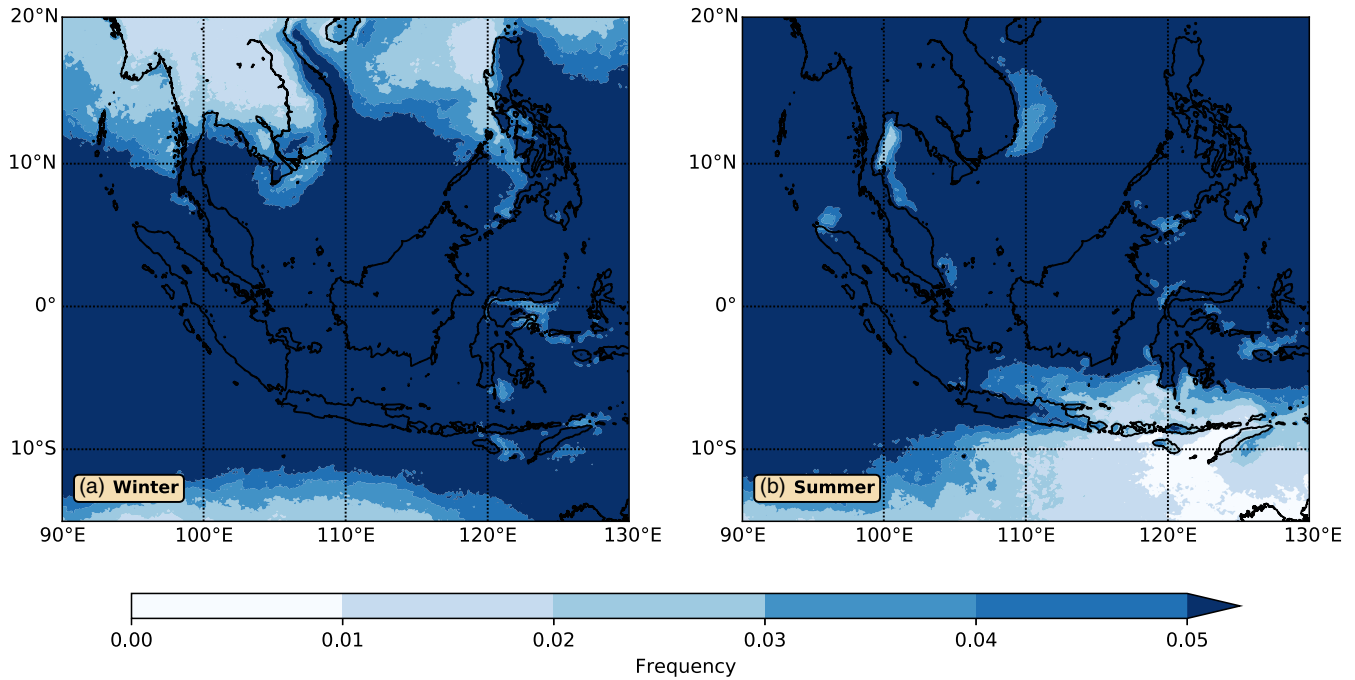
FIGURE 4 Reference frequency f_0 of observing daily extreme precipitation (above the 95th percentile of grid point precipitation, and above an absolute threshold of 20 mm·day^{-1}) during (a) boreal winter (October–March), (b) boreal summer (April–September). Note that the maximum possible value of f_0 is exactly 0.05 (dark-blue shading) [Colour figure can be viewed at wileyonlinelibrary.com]

areas there experience enhanced precipitation. The magnitude of these positive precipitation anomalies is typically 4–8 mm·day^{-1}, representing a modulation of the mean precipitation (Figure 2a) of over 50%. During phase 5 (Figure 3e), a vanguard of suppressed precipitation advances along the equator to cover Sumatra, Borneo, Java and Sulawesi, while the surrounding oceanic regions are still experiencing wet conditions. During phases 6, 7 and 8 (Figure 3f–h), the main envelope of suppressed convection covers the western MC, as the active part of the MJO moves eastward and poleward over the western Pacific. Finally, a composite precipitation anomaly from all the days in which there is no MJO activity (Figure 3i), defined as the magnitude of the OMI index being less than one, shows very weak anomalies with no coherent structure.

4.2 | Methodology

To quantify the change of precipitation frequency with MJO phase, the observed 'reference' frequencies f_0 of extreme precipitation events over both boreal winters (Figure 4a) and boreal summers (Figure 4b) for the whole study period (2001–2019) was first calculated. By construction, this equals 0.05 over most of the domain, but is lower over the northern parts of the western MC (mainly during boreal winter) and over the southern parts of the western MC (mainly during boreal summer) because of the

additional absolute 20 mm·day^{-1} threshold. The observed frequency of extreme precipitation within each individual MJO phase f_p was then calculated. Then, the ratio, or relative frequency

$$R_p = \frac{f_p}{f_0} \qquad (1)$$

was calculated to examine the change of frequency of extreme precipitation within each MJO phase. A value of $R_p > 1$ indicates that extreme precipitation is more likely in a particular MJO phase, whereas $R_p < 1$ indicates that extreme precipitation is less likely.

To evaluate if the change of frequency R_p is significant, a statistical test was performed following Hall *et al.* (2001). For each MJO phase, the null hypothesis is that the probability of occurrence of an extreme precipitation event is not changed. The test statistic Z_p is defined as

$$Z_p = \frac{f_p - f_0}{s}, \qquad (2)$$

where $s = \sqrt{f_0(1 - f_0)/N}$ is an estimator of the standard deviation of the frequency of extreme precipitation days, and N is the number of days in that MJO phase (Table 1). Under the null hypothesis, the test statistic Z_p is distributed according to a binomial distribution, which approximates to the standard normal distribution here because of the large number of events ($N \approx 200$). Hence, in a two-tailed test at the 5% level, the frequency of observing

TABLE 1 Number of days N in each MJO phase and boreal season

MJO phase	Winter	Summer	Total
1	229	207	436
2	274	323	597
3	313	276	589
4	264	157	421
5	215	243	458
6	273	307	580
7	289	240	529
8	288	180	468
None	1,317	1,544	2,861
Total	3,462	3,477	6,939

precipitation extremes in a particular MJO phase is said to be significantly different from the mean frequency of precipitation extremes when $Z < -1.96$ or $Z > 1.96$. In practice, for $f_0 = 0.05$ and $N = 200$, then $s = 0.0154$, and for significance at the 5% level, then $f_p < 0.020$ or $f_p > 0.080$, and $R_p < 0.40$ or $R_p > 1.60$. Hence, there must be at least an approximate 60% decrease or increase in the relative frequency of observing extreme weather in a particular MJO phase for the effect to be statistically significant. This significance level will vary slightly because the number of days N in each MJO phase varies, and in the far northern and southern parts of the domain where $f_0 < 0.05$.

4.3 | Spatial patterns of extreme precipitation within the MJO

Maps of this relative frequency R_p in each MJO phase show that the MJO exerts a large and significant impact on the probability of observing extreme precipitation in both seasons (Figures 5 and 6). The spatial patterns of extreme precipitation frequencies in both seasons (Figures 5 and 6) approximately follow those of the mean annual precipitation anomalies (Figure 3), with some noticeable changes according to season. During MJO phase 1–2, the probability of observing extreme precipitation in the convectively suppressed regions along 10° N and 10° S is reduced to below $R_p = 0.5$ of its reference value (Figures 5a and 6a), that is, a 50% decrease, with significant areas with $R_p < 0.33$, a 67% decrease. On the equator, off the western coast of Sumatra and over the Karimata Strait between Sumatra and Borneo, there is an enhanced probability of extreme precipitation ($R_p > 1.4$, a 40% increase), consistent with the vanguard of precipitation there at this time. We note that the vanguard signal is also present during boreal summer, showing that this a pattern of both the BSISO and the MJO.

As the MJO/BSISO envelope of convection moves eastward and poleward, so too does the change in probability of observing extreme precipitation. Large regions where $R_p > 2$ (a 100% increase in probability of extreme precipitation) are observed: over the equatorial eastern Indian Ocean during phase 2–3 (Figures 5b,c and 6b,c); to the south of Java, over the Java Sea, Banda Sea and Molucca Sea during phase 4 (Figures 5d and 6d); and over the South China Sea, the Philippines and the Philippine Sea, and over the Timor Sea during phases 4 and 5 (Figures 5d,e and 6d,e). Similarly, large regions where $R_p < 0.50$ (a two-fold decrease in probability of extreme precipitation) are observed: the Banda Sea and Timor Sea during phases 1, 2 and 3 (Figures 5a–c and 6a–c); the Karimata Strait and western Borneo in phases 6 and 7 (Figures 5f,g and 6f,g); the eastern Indian Ocean during phases 6, 7 and 8 (Figures 5f–h and 6f–h); the South China Sea during phases 8, 1, 2 and 3 (Figures 5a–c,h and 6a–c,h).

Using the TRMM satellite precipitation data, Xavier *et al.* (2014) did not identify any increase of precipitation extremes during MJO phases 2–4 in both eastern Peninsular Malaysia and north-west Borneo for the winter season (November–March). In contrast, our results show that the MJO influences the probability of extreme precipitation in these regions. Such qualitative differences may be related to their merging of MJO phases 2–4 and/or the reduced spatio-temporal resolution of TRMM compared with GPM IMERG.

The modulation of precipitation extreme frequency by the BSISO appears to be more pronounced during boreal summer than by the MJO during boreal winter for all regions to the north of 5° S, with a slight northward shift of the patterns in this season. The reverse is true for regions south of 5° S, where the BSISO has less impact in boreal summer than the MJO does in boreal winter. This is consistent with the southward 'detour' of the MJO in boreal winter (Kim *et al.*, 2017), compared with the BSISO in summer, and the northward propagation of the BSISO.

In general, the whole of the western MC experiences increased probability of extreme precipitation during phase 4 (Figures 5d and 6d) and decreased probability during phase 8 (Figures 5h and 6h). As expected, there are only small, incoherent areas of weakly enhanced or reduced probability of extreme precipitation when the MJO is inactive (Figures 5i and 6i).

4.4 | Effect of topography and season on extreme precipitation within the MJO

In this section, we investigate the effect of land–sea contrasts and topography on extreme precipitation in the MJO, and also the importance of the seasonal cycle. Here, R_p
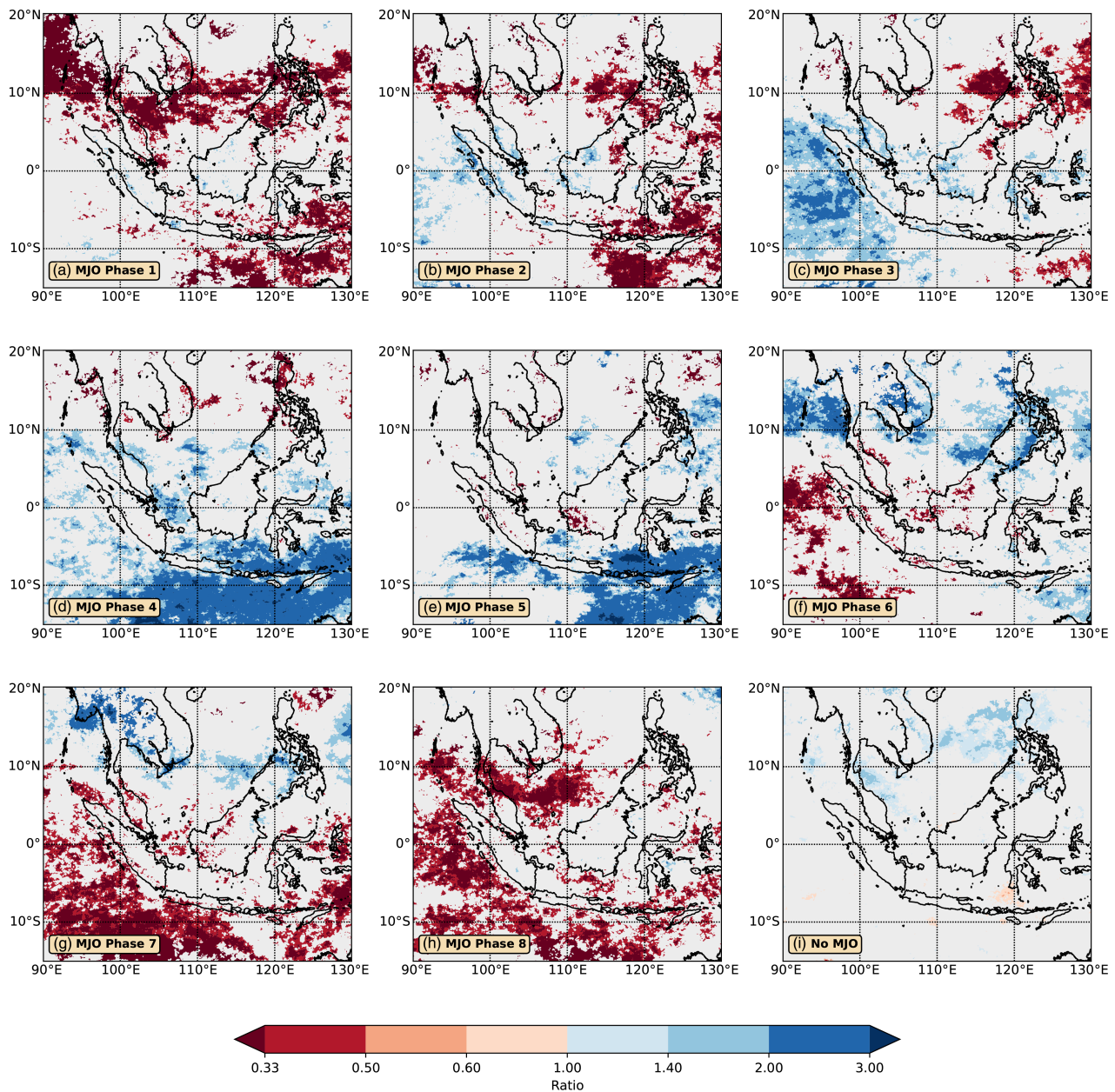
FIGURE 5 Ratio R_p of frequency of observing daily extreme precipitation in a particular MJO phase during boreal winter (October–March) [Colour figure can be viewed at wileyonlinelibrary.com]

ratios were averaged over the nine specific regions of particularly high extreme precipitation identified in Section 3: northern Myanmar, southern Myanmar, western Cambodia, eastern Peninsular Malaysia, north-western Philippines, eastern Philippines, western Sumatra, north-west Borneo and eastern Sulawesi (black boxes in Figures 1 and 2a,b).

In addition to calculating R_p values for the standard 95th percentile chosen for extreme precipitation, R_p values were also calculated for: (a) exceedance of both the 99th percentile and the absolute 20 mm·day^{-1} threshold, as a measure of even more extreme precipitation, and (b) exceedance of the median (50th percentile), with no

absolute threshold, as a measure of the change in average precipitation by the MJO for comparison with changes in extreme precipitation.

Grid points within each of these boxes were classified into three categories using the mean topographic altitude averaged over the relevant IMERG grid box: (a) lowland, altitude between 0 and 500 m, (b) mountain, altitude above 500 m and (c) sea, with altitude not exceeding 0 m. Differences between the MJO signal in average precipitation have already been identified between land and sea (Peatman *et al.*, 2014) and between lowland and mountainous regions (Matthews *et al.*, 2013). Hence, the distinction was made here to investigate whether this also applies to MJO
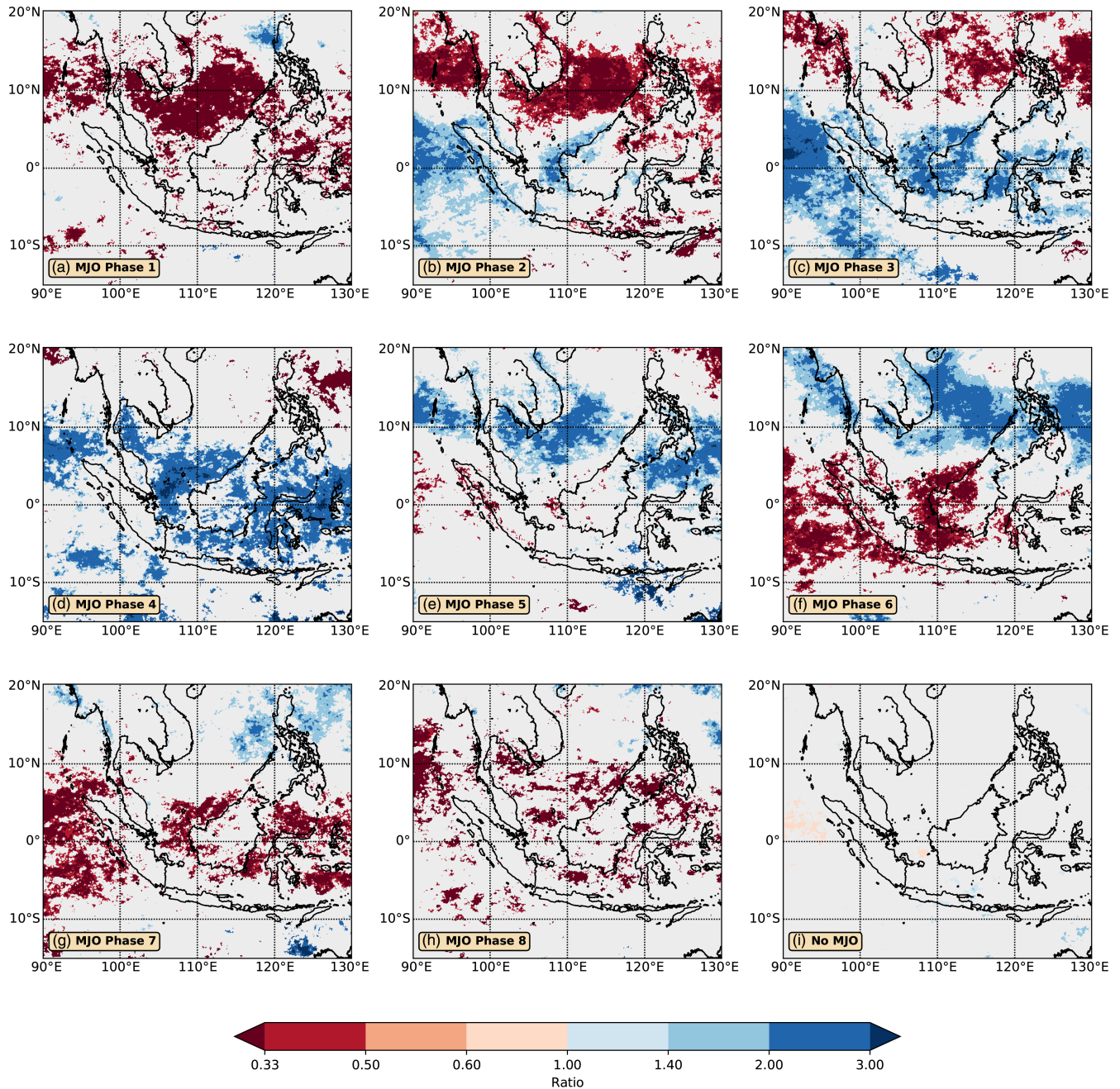
FIGURE 6 As Figure 5 but for boreal summer (April–September) [Colour figure can be viewed at wileyonlinelibrary.com]

changes in extreme precipitation. Additionally, the majority of the population in the MC live in lowland areas (Gaughan *et al.*, 2013), so any differences between lowland regions and mountain or sea will be important for societal impacts.

4.4.1 | Lowland regions

To take into account the potential influence of season on the MJO impact on precipitation extremes, analyses were done separately for October–March (boreal winter) and

for April–September (boreal summer). For each region and season, the median of the R_p ratios is plotted against MJO phase for lowland grid points in Figure 7). Clear MJO cycles in extreme precipitation can be seen in each of the nine regions; note that statistically significant values are denoted by the large markers. In general, the ratios for extreme precipitation (95th percentile, dashed lines in Figure 7; 99th percentile, dash–dot lines in Figure 7) deviate more from the reference ratio $R_p = 1$ than the ratios for the median precipitation (50th percentile, solid lines in Figure 7). This implies that the MJO has a larger impact on the occurrence of extreme precipitation than it does
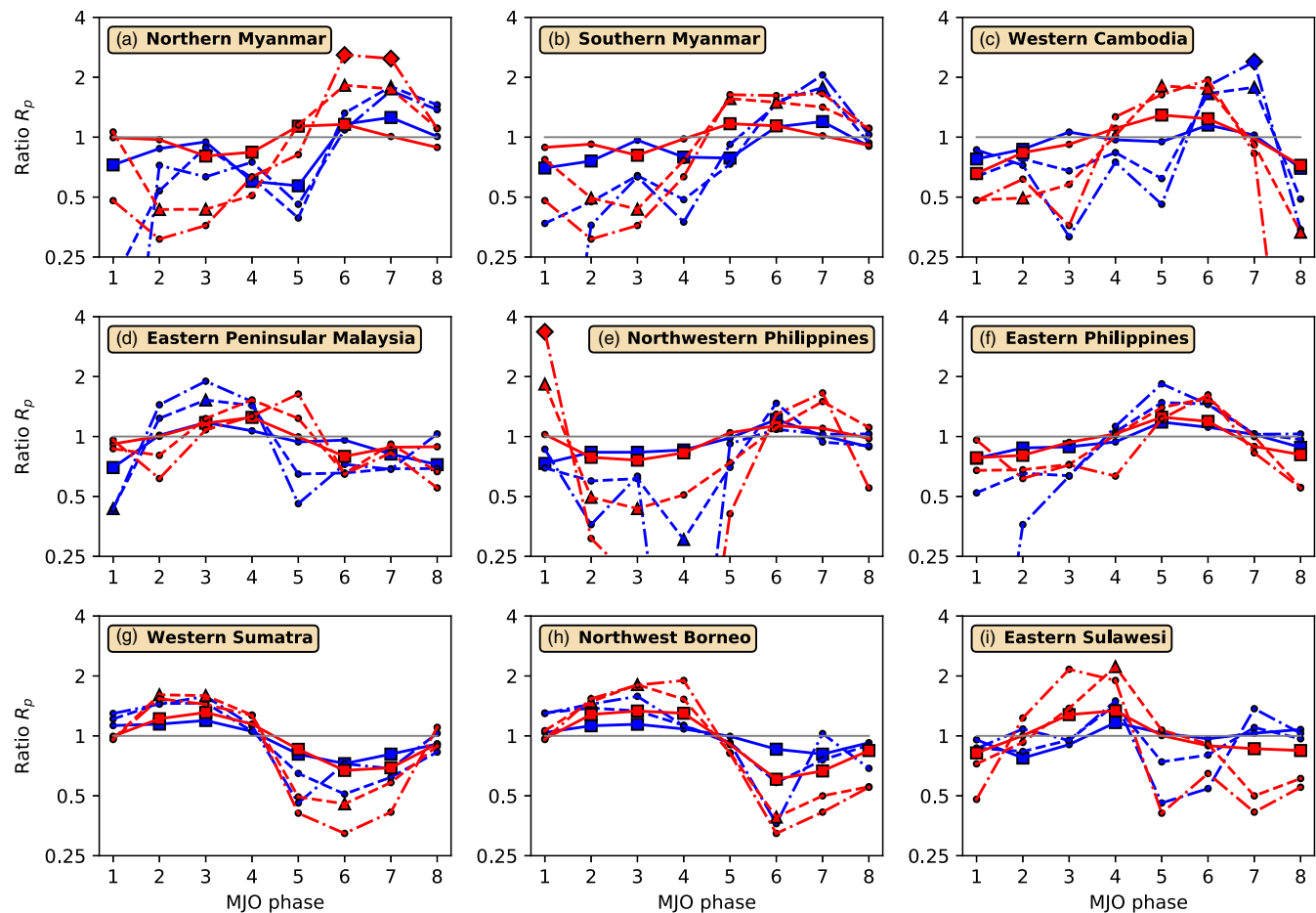
FIGURE 7 Median of ratio R_p of frequency of observing daily precipitation above a fixed percentile (50th in solid, 95th in dashed, 99th in dash-dotted) to the reference frequency, for lowland grid points only (elevation between 0 and 500 m), as a function of MJO phase, for the October–March period (blue) and the April–September period (red) in the nine selected high-precipitation areas. Values that are statistically significant at the 95% level are shown by large markers: square for 50th percentile, triangle for 95th percentile, diamond for 99th percentile [Colour figure can be viewed at wileyonlinelibrary.com]

on average precipitation. Even though all nine regions are in the western MC, where the large-scale envelope of the MJO is in its enhanced convective phase during phases 3, 4 and 5 (Wheeler and Hendon, 2004), there is considerable variation in the peak phase for extreme precipitation between the region, from as early as phase 2 for western Sumatra (Figure 7g) to as late as phase 1 for the north-western Philippines (Figure 7e).

Northern Myanmar (at 16–20° N) shows a strong BSISO cycle in extreme precipitation during boreal summer (red lines in Figure 7a), with significantly reduced occurrence of extreme precipitation in phase 2–3 and increased occurrence in phase 6–7, the latter being significant for the 99th percentile of precipitation extremes.

During boreal winter (blue lines in Figure 7a), there are no significant changes in extreme precipitation during the MJO cycle, but the cycle of median precipitation has shifted from summer, with a minimum in phase 5 rather than 3. However, note that the reference frequency f_0 is

below 0.02 here in winter, hence there are very few extreme events.

In southern Myanmar, the peak of extreme precipitation frequency occurs at an earlier stage (phases 5–6) of the BSISO cycle during boreal summer and with a reduced amplitude (red lines in Figure 7b). The signal is similar in western Cambodia, which also exhibits a more pronounced increase of precipitation extreme frequency in MJO phase 7 during boreal winter (significant for the 99th percentile; Figure 7c).

Conversely to the previous northern regions, eastern Peninsular Malaysia displays a peak of average precipitation earlier in the MJO cycle during boreal winter (MJO phase 3) than during boreal summer (phase 4). The changes of extreme precipitation frequency are significant only during boreal winter, with a reduction in MJO phase 1 and an increase in MJO phase 3.

The MJO cycle of extreme precipitation in the north-western Philippines is large during boreal summer
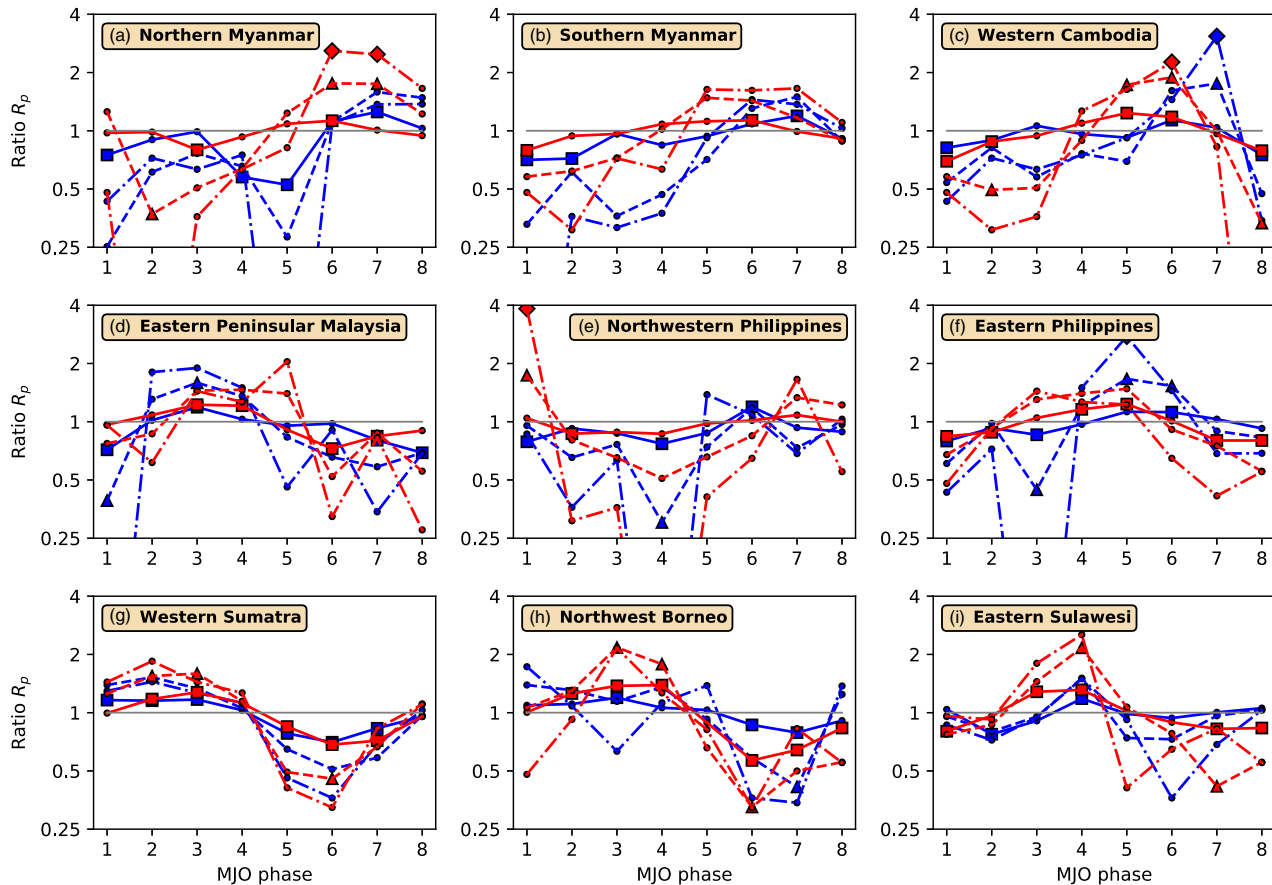
FIGURE 8   As Figure 7 but for mountain grid points [Colour figure can be viewed at wileyonlinelibrary.com]

(red lines in Figure 7e), with suppressed extreme precipitation in MJO phases 2–5 (significant in phases 2–3) and a sharp increase during MJO phase 1, for which very extreme precipitation (99th percentile) is nearly four times more frequent. This feature is not present during boreal winter (blue lines in Figure 7e), where average precipitation and precipitation extremes are mostly reduced by the MJO. The MJO has no significant impact on extreme rainfall in the eastern Philippines in boreal winter but does significantly increase their frequency in MJO phase 6 during boreal summer (Figure 7f).

The MJO cycle for extreme precipitation over western Sumatra follows the cycle for average (median) precipitation (Figure 7g), with a statistically significant increase in the probability of extreme precipitation in phases 2 and 3 and a decrease in phase 6, both during boreal summer. The cycle displays a similar behaviour during boreal winter, but the peaks are no longer significant. Over north-west Borneo, the MJO cycle of precipitation is similar to that of western Sumatra, with a significant increase in the probability of extreme precipitation in phases 2 and 3 and a reduction in phases 5 and 6 of boreal summer (Figure 7h).

For eastern Sulawesi, there are significant increases in extreme precipitation during MJO phase 4 in boreal

summer (red lines in Figure 7i), commensurate with the standard large-scale envelope of MJO convection over the MC. However, no significant changes in precipitation are observed here in boreal winter.

In general, changes in extreme precipitation at the 99th percentile tracked those at the 95th percentile, but were noisier and less robust, and less likely to be statistically significant. This indicates that the limits of the finite observational dataset are being reached when analysing these very extreme events.

4.4.2 | Mountain regions

The analysis was repeated but just using the mountain grid points (elevation above 500 m) for each of the nine regions (Figure 8). Perhaps surprisingly, there was little qualitative difference between the MJO cycles in extreme precipitation in the mountain and lowland grid points. However, the robustness of the precipitation extreme changes due to the MJO may differ between lowland and mountain grid points.

The signal-to-noise ratio is enhanced for phase 6 in boreal summer in western Cambodia (Figure 8c), for phase
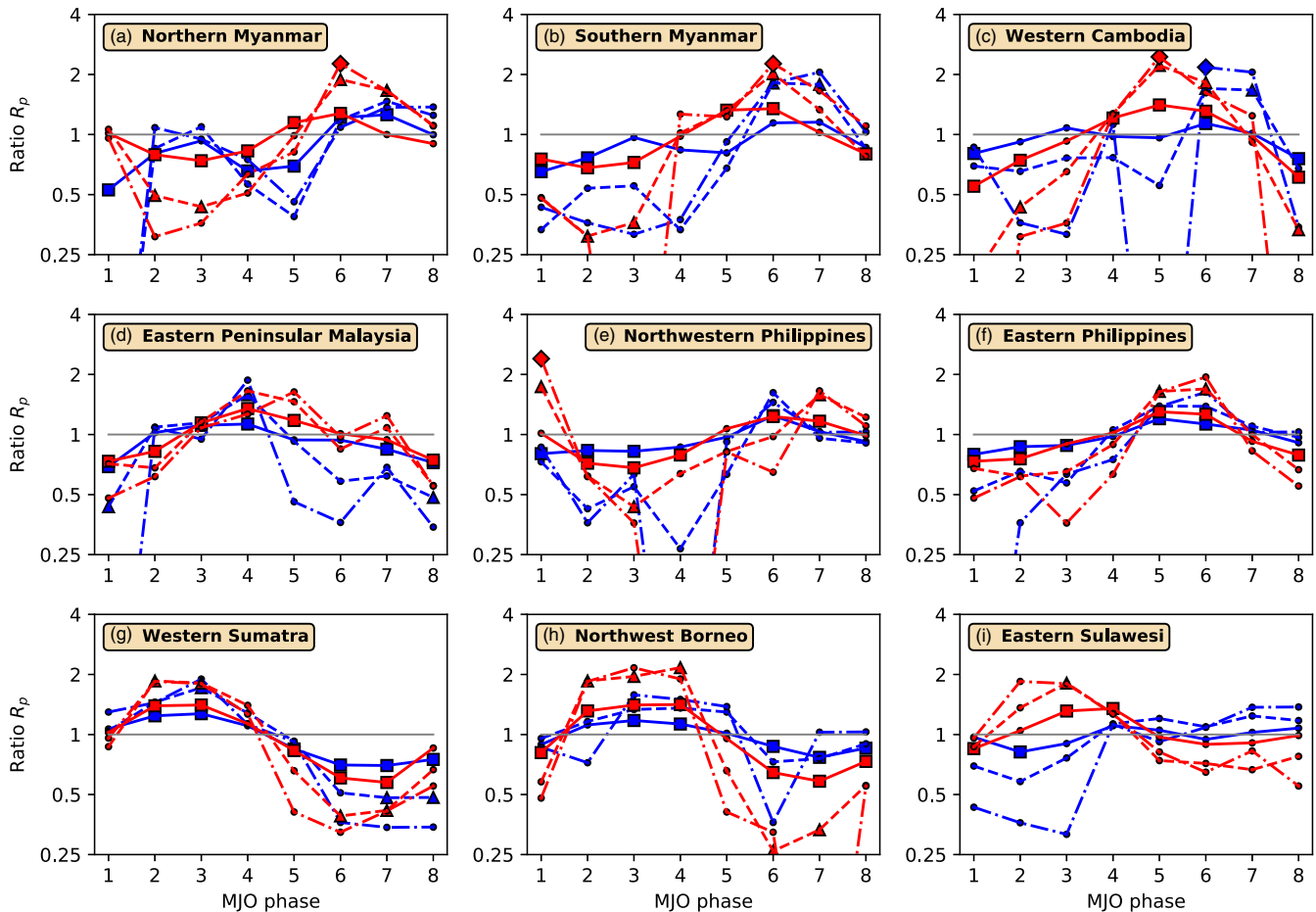
FIGURE 9   As Figure 7 but for sea grid points [Colour figure can be viewed at wileyonlinelibrary.com]

4 in boreal summer in north-west Borneo (Figure 8h) and for phase 5 in boreal winter in eastern Philippines (Figure 8f). Conversely, the increased frequency of extreme precipitation events in southern Myanmar is no more significant for mountain grid points in MJO phase 5–6 during boreal summer. Finally, the boreal summer peak of precipitation extremes in eastern Philippines in MJO phase 5 disappeared for mountain grid points.

4.4.3 | Ocean regions

The analysis was repeated again, but just using the ocean/sea grid points for each of the nine regions. Qualitative differences in the behaviour of the MJO cycle in extreme precipitation were observed between the ocean and the land. Sea grid points in the region of southern Myanmar and in the region of western Cambodia (Figure 9b,c) display a significant peak frequency of very extreme precipitation (above the 99th percentile) during MJO phase 6 and 5 (respectively) in boreal summer. In the same regions, the boreal winter peak of precipitation

extreme frequency tends to occur one phase earlier (in phase 6) than for the lowland grid points.

The frequency of extreme precipitation in the sea grid points of eastern Peninsular Malaysia does not significantly change for each phase of the MJO during boreal summer, an observation also valid for the lowland grid points. In boreal winter, however, the significant peak frequency of extreme precipitation during phase 3 of the MJO in lowland and mountain grid points is present in MJO phase 4 for the sea grid points. This is reminiscent of the vanguard of precipitation which mostly affects the western coast of Sumatra, and the north-western coast of Borneo ahead of the main MJO core envelope (Peatman *et al.*, 2014; Birch *et al.*, 2016). For the case of eastern Peninsular Malaysia, the presence of the MJO core in the west of this region may enhance north-easterly flow (Xavier *et al.*, 2014) and create extreme precipitation through mechanically forced convection (Wang and Sobel, 2017).

The situation is the reverse in eastern Sulawesi, where the peak of precipitation extreme frequency is one phase earlier (BSISO phase 3) for the sea grid points than for the lowland grid points (BSISO phase 4) in boreal summer.
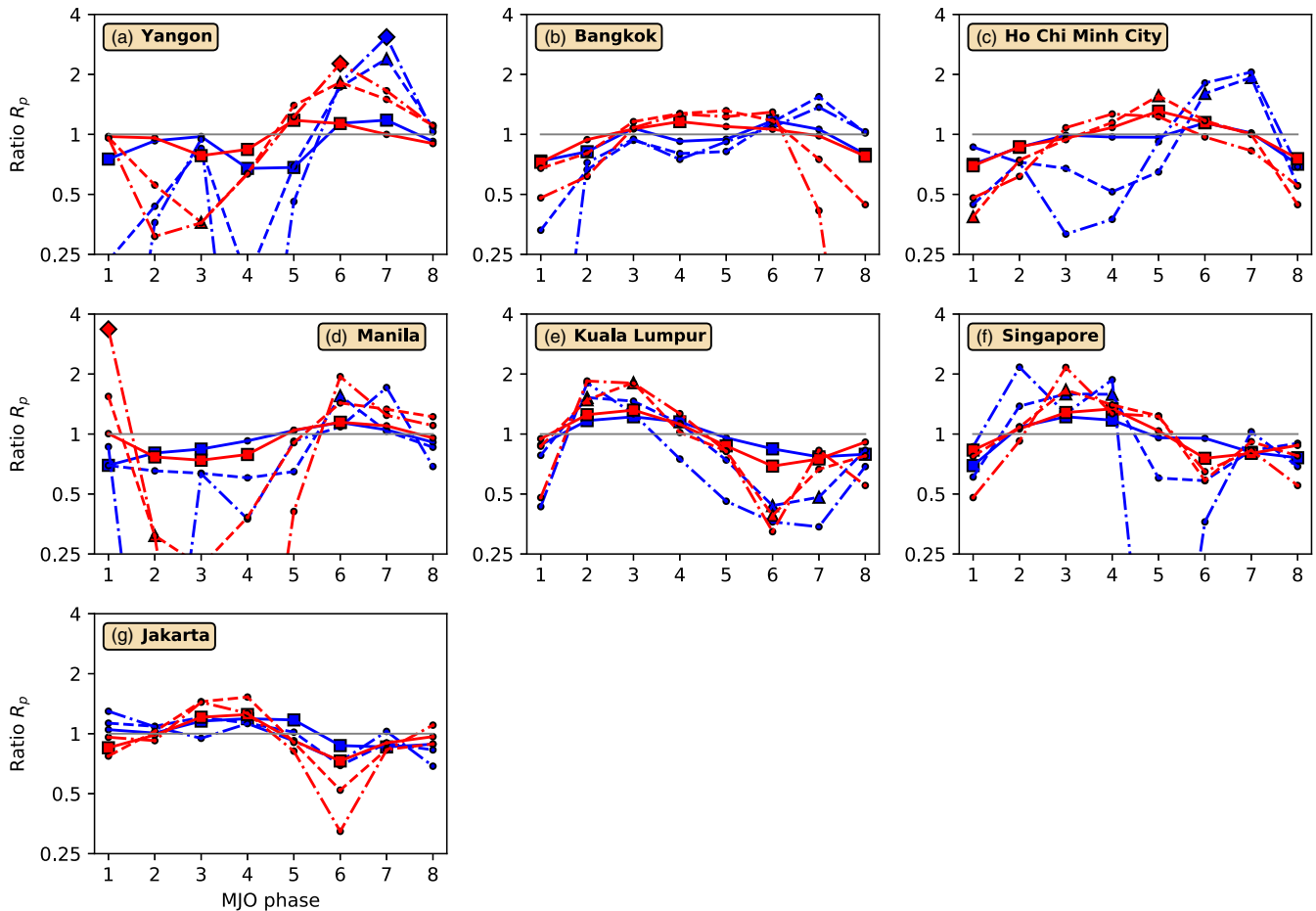
FIGURE 10 Ratio R_p of frequency of observing daily precipitation above a fixed percentile (50th in solid, 95th in dashed, 99th in dash-dotted) to the reference frequency, as a function of MJO phase, for the October–March period (blue) and the April–September period (red) in the seven selected major cities [Colour figure can be viewed at wileyonlinelibrary.com]

4.5 | Impact of the MJO on extreme precipitation over the major cities of the western MC

The analysis in Section 4.4 was conducted over the main areas of extreme precipitation in the western MC, as identified in Figure 2b. However, these regions are generally not the most populated areas (Gaughan *et al.*, 2013). Hence, a similar analysis is now carried out for the main population centres in the western MC to assess the main societally relevant impact of the MJO on extreme precipitation. The cities chosen are: Manila (population 24 million), Jakarta (29 million), Bangkok (17 million), Ho Chi Minh City (8 million), Kuala Lumpur (7 million), Singapore (7 million) and Yangon (7 million). The corresponding regions that were selected are indicated by magenta boxes in Figures 1, 2a,b. No distinction was made between lowland, mountain and sea grid points. We note that these city areas (magenta boxes) are much smaller than the physical centres of high precipitation analysed in Section 4.4 (black boxes), hence the results are not as robust and prone to fluctuations.

Nevertheless, the analysis provides a useful indication on what can be typically expected from the MJO on a city scale.

Yangon (Figure 10a) shows a similar pattern to northern Myanmar, with twice the probability of very extreme precipitation during MJO phase 6 during boreal summer, but also a significant, three-fold increase of very extreme precipitation during boreal winter in MJO phase 7. Bangkok (Figure 10b) shows no significantly increased probability of extreme precipitation during the MJO. Extreme precipitation changes in Ho Chi Minh City (Figure 10c) are similar to those in nearby western Cambodia, with a 50–80% increase in MJO phases 6–7 during boreal winter, and a slightly lower increase in summer in MJO phase 5. The results for Manila (Figure 10d) reflect the north-western Philippines region it is embedded in, and show up to a three-fold increase in the probability of very extreme precipitation during MJO phase 1 during boreal summer, and a 50% increase of extreme precipitation in MJO phase 6 during boreal winter. Kuala Lumpur (Figure 10e) has a maximum frequency
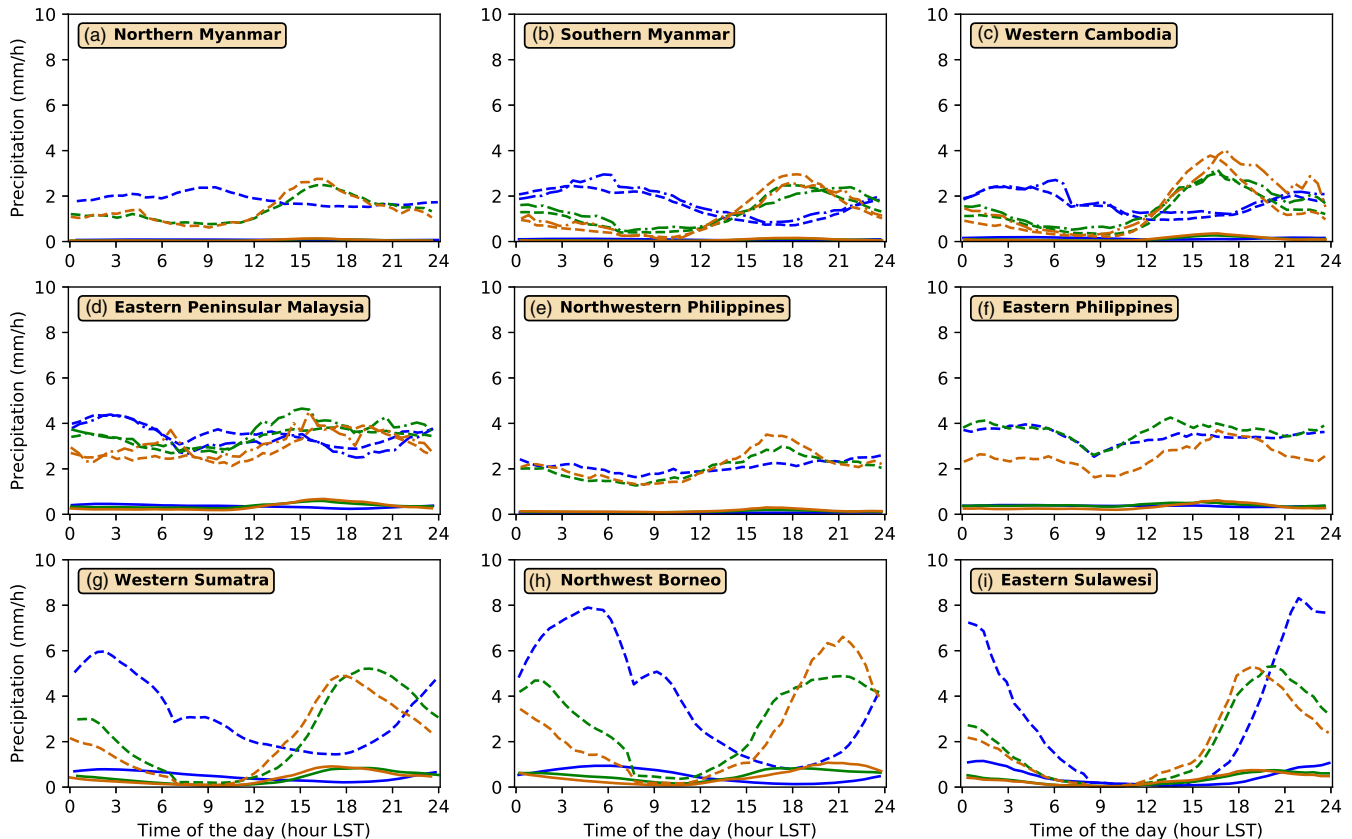
FIGURE 11 Diurnal cycle for boreal winter for each of the nine high-precipitation regions. Blue, green and brown lines correspond to ocean, lowland and mountain grid points, respectively, in each area. The solid line is the mean diurnal cycle calculated over all days for that region. The dashed line is the diurnal cycle calculated over all extreme precipitation days. The dash-dotted line is the diurnal cycle calculated over the extreme precipitation days that occurred in the MJO active phase for that region (Table 2); if no active phase was defined, then no diurnal cycle is plotted [Colour figure can be viewed at wileyonlinelibrary.com]

of extreme precipitation during phases 2–3 in both summer and winter. Although it is very close geographically, Singapore (Figure 10f) experiences a significant increase of precipitation extremes one phase later, in MJO phases 3–4 during both seasons. Finally, although Jakarta (Figure 10g) has a significant MJO cycle in median precipitation, it does not experience any significant changes in extreme precipitation during the MJO.

5 | DIURNAL CYCLE ON EXTREME PRECIPITATION DAYS AND MODULATION BY THE MJO

5.1 | Mean diurnal cycle and diurnal cycle on extreme precipitation days

The diurnal cycle of precipitation is particularly strong over the MC (Yang and Slingo, 2001; Love *et al.*, 2011). However, it is not clear if the diurnal cycle is a key ingredient of extreme precipitation days: is the diurnal cycle swamped by large-scale weather systems, or is it

enhanced? Hence, two versions of the diurnal cycle were calculated. First, the mean diurnal cycle was calculated for each of the high-rainfall regions, separately for lowland, mountain and ocean grid points (solid lines in Figure 11 for boreal winter and Figure 12 for summer). Second, the diurnal cycle was recalculated for each region, but only using the extreme precipitation days (dashed lines in Figures 11 and 12).

In most locations, the diurnal cycle on extreme precipitation days (dashed lines) is an amplified version of the mean diurnal cycle (solid lines). For example, over north-west Borneo in boreal winter (Figure 11h), the mean diurnal cycle shows its expected behaviour with a peak in the late afternoon (1800 LST) over the lowland region (green solid line). Over the mountain region (brown solid line), the peak is later at approximately 2100 LST, consistent with the migration of the peak rainfall inland from the coastal lowlands to the mountains in the interior (Love *et al.*, 2011). In contrast, the peak over the ocean region (blue solid line) is in the early morning at 0600 LST.

This preservation of the diurnal cycle during these extreme precipitation days shows the fundamental role
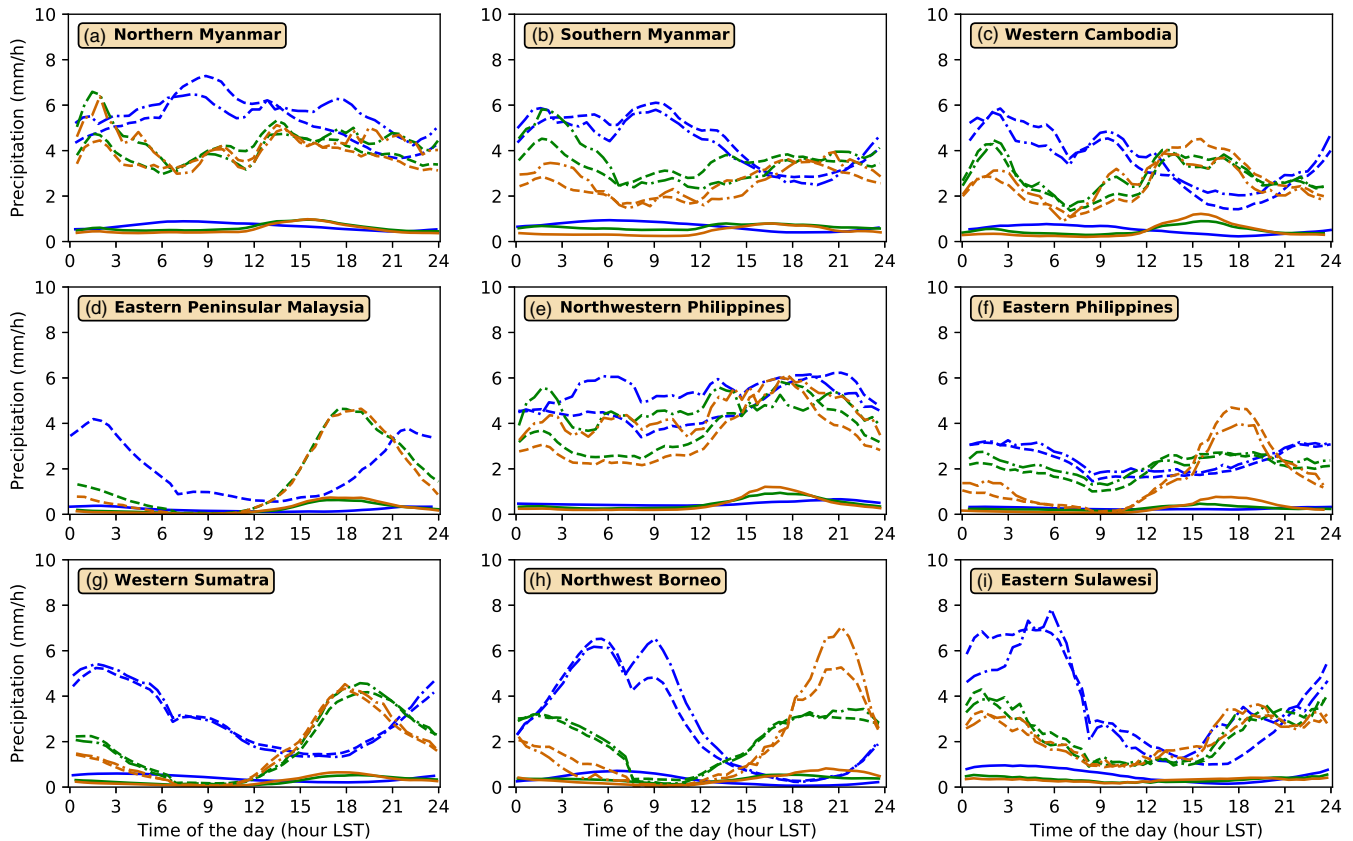
FIGURE 12 As Figure 11 but for boreal summer [Colour figure can be viewed at wileyonlinelibrary.com]

TABLE 2 MJO active phase for extreme precipitation, for each of the nine selected high-precipitation areas for boreal winter (October–March) and summer (April–September) seasons

Location	Winter	Summer
Northern Myanmar	–	6 (99th)
Southern Myanmar	7 (95th)	5 (95th)
Western Cambodia	7 (99th)	5 (95th)
Eastern Peninsular Malaysia	3 (95th)	–
North-western Philippines	–	1 (99th)
Eastern Philippines	–	6 (95th)
Western Sumatra	–	2 (95th)
North-west Borneo	–	3 (95th)
Eastern Sulawesi	–	4 (95th)

Note: The percentile from Figure 7 used to select the active phase is shown in brackets. A dash indicates that no active phase is defined (no phase significant at the 95th percentile).

that the diurnal cycle plays over the MC. It is certainly not the case that the diurnal cycle is just a 'default' pattern that is obliterated by larger-scale forcing during extreme weather. Instead, the extreme weather forcing interacts with and amplifies the underlying diurnal signal. Recent

studies have shown that large-scale dynamics may impact not only the amplitude but also the timing of the diurnal cycle of precipitation in these tropical islands (Wang and Sobel, 2017; Zhu *et al.*, 2020). While this latter characteristic may occur in some individual extreme weather events, our study suggests that most of the extreme weather forcing does not offset the diurnal cycle of precipitation in the MC.

This amplification of the diurnal cycle on extreme precipitation days is mirrored to a greater or lesser extent across all the regions. The diurnal cycle is particularly strong over the large equatorial island regions of western Sumatra, north-west Borneo and eastern Sulawesi (Figures 11 and 12g–i), with relatively little seasonal dependence, as there are no clear wet and dry seasons here. The diurnal cycle is rather pronounced in boreal winter over the boreal regions of northern Myanmar, southern Myanmar and western Cambodia, during their dry season (Figure 11a–c), and weaker in their wet season during boreal summer (Figure 12a–c). Eastern Peninsular Malaysia exhibits similar behaviour, with a weak diurnal cycle in boreal winter (Figure 11d) and a strong diurnal cycle in boreal summer (Figure 12d), even though there is little seasonal difference in total rainfall. The suppression of the diurnal cycle during boreal winter is consistent

with the findings of Jamaluddin *et al.* (2018), who found that an increase in cloud cover during daytime in the north-easterly monsoon flow stabilised the atmosphere, decreasing the amount of convection during the daytime and hence reducing the amplitude of the diurnal cycle.

The two Philippines regions experience a greater proportion of large-scale organised weather systems such as tropical cyclones and typhoons (Prat and Nelson, 2013), and have much weaker diurnal cycles (Figures 11 and 12e,f) (Bowman and Fowler, 2015), especially in boreal winter.

5.2 | Diurnal cycle on extreme precipitation days within the MJO active phase

The MJO is known to have a significant impact on the amplitude of the mean diurnal cycle of rainfall (Oh *et al.*, 2012; Peatman *et al.*, 2014). Hence, in addition to affecting the frequency of daily extreme precipitation (Section 4), the MJO may also have an effect on the amplitude of the diurnal cycle of these extreme precipitation events. Additionally, there may be an impact on the timing of the diurnal cycle. Previous studies have typically used the TRMM rainfall dataset, which has only 3-hourly time resolution. It is unlikely that a change in timing of the diurnal cycle would be as large as 3 hrs, hence previous analyses would have been unable to detect any such change. Here, we take advantage of the 30-min time resolution of the GPM IMERG dataset to investigate whether the MJO exerts a change in the timing of the diurnal cycle during extreme precipitation events.

To address this issue, we first define the most 'active' MJO phase for extreme precipitation (Table 2) for each of the nine selected high-precipitation areas (black boxes in Figure 1). The active MJO phase for extreme precipitation for a region is defined as the phase in which the extreme precipitation ratio R_p for lowland grid points (calculated using the 99th percentile, that is, from the dash-dotted lines in Figure 7) is a maximum. However, if this is not statistically significant (no large marker at the relevant point in Figure 7), the ratio using the 95th percentile is used instead (i.e. from the dashed lines in Figure 7). If this is not significant, then no active MJO phase for extreme precipitation is defined.

We then calculate a third version of the diurnal cycle, using only the extreme precipitation days within the active MJO phase for that region (dot-dashed lines in Figures 11 and 12). In general, there is very little difference between the diurnal cycle on extreme precipitation days during the active MJO (dot-dashed lines in Figures 11 and 12), compared with the diurnal cycle from all extreme precipitation days, regardless of MJO phase (dashed lines in Figures 11 and 12). This similarity applies to both the amplitude and timing of the diurnal cycle.

For example, for lowland north-west Borneo in boreal summer, the frequency of extreme precipitation days during the active MJO (phase 3) is $R_p = 1.5$ times higher than the background frequency. This is significant at the 95th percentile (red dashed line in Figure 7h; Table 2). However, the diurnal cycle on extreme precipitation days in MJO phase 3 (green dot-dashed line in Figure 12h) is almost identical to the diurnal cycle over all extreme precipitation days (green dashed line in Figure 12h). The interpretation is that, while an active MJO makes extreme precipitation days more likely to occur, it does not increase either the total amount of rain that falls on those extreme precipitation days or the diurnal variability. A similar pattern is observed for the ocean grid points in north-west Borneo (blue dot-dashed and dashed lines in Figure 12h). There is, however, a slight increase in the amplitude of the diurnal cycle over the mountain grid points in north-west Borneo (brown dot-dashed and dashed lines in Figure 12h), but not in the daily total.

The similarity between the diurnal cycle on extreme precipitation days in the MJO active phase and the diurnal cycle on all extreme precipitation days persists across the islands of the equatorial MC in boreal summer: western Sumatra, north-west Borneo and eastern Sulawesi (Figure 12g–i). The remaining locations (Figures 11 and 12a–f) where an active MJO phase was defined also generally conform to this similarity. One may, however, notice that precipitation extremes are more intense in the north-western Philippines during the MJO active phase of boreal summer (phase 1) and increased precipitation extreme intensities during the first hours of the day in the boreal summer MJO active phase of both northern and southern Myanmar (Figure 12a,b).

6 | CONCLUSIONS

We have presented an analysis of the effect of the MJO on extreme precipitation over the western MC. The availability of the GPM IMERG dataset allowed this to be carried out at far higher spatial and temporal resolution than previously. Extreme rainfall was defined locally, at the grid point scale, when the daily total precipitation exceeded a percentile (either the 95th or 99th) of the daily precipitation distribution, and also an absolute threshold (set to 20 mm·day^{-1}). Statistical significance was assessed with the use of a normality test. Our analysis confirmed the great influence that the MJO has on precipitation extremes in the MC. The MJO impact on precipitation was found to be stronger for extreme precipitation than for average

precipitation in each of the nine selected areas of high precipitation in the MC. The frequency of observing an extreme rainfall day increased significantly, by over a factor of 2 over large areas during the MJO active convection phase. Similarly, it decreased by more than a factor of 0.5 over large areas during the MJO suppressed phase.

However, the pattern of extreme precipitation within each MJO phase shows spatial complexity. It is not the case that a blanket statement can be made such as extreme precipitation being more likely across the western MC during phases 2–4. Instead, the pattern of extreme precipitation is strongly tied to the complex distribution of land, sea and topography, much as the pattern of mean rainfall is within the MJO (Peatman *et al.*, 2014; Birch *et al.*, 2016). This feature may explain why we found significant changes of extreme precipitation frequencies within the MJO in north-west Borneo and eastern Peninsular Malaysia during boreal winter, in contrast to the findings of Xavier *et al.* (2014), whose TRMM extreme precipitation frequencies were averaged for MJO phase 2–4. In boreal winter, the sensitivity of precipitation extremes to the phase of the MJO is higher in the Southern Hemisphere, consistent with the MJO 'detour' observed in this season (Kim *et al.*, 2017). Conversely, the BSISO has more impact on extreme precipitation frequency in the Northern Hemisphere during summer and is associated with a slight northward shift of the patterns.

For this analysis, a distinction was made between lowland (below 500 m elevation), mountain (above 500 m) and ocean/sea regions, as physical controls on precipitation may be different between these regions, and the main population centres are in lowland regions, so a more discriminatory analysis will allow results to be applied in a more socially useful manner. Over the lowland regions, in MJO phase 2–3, a vanguard of extreme precipitation propagates into the equatorial first (western Sumatra, eastern Peninsular Malaysia and north-west Borneo), reaching eastern Sulawesi in phase 4, then expanding northward into western Cambodia and southern Myanmar in phases 5–6, and northern Myanmar in phase 6. The frequency of extreme rainfall peaks in the eastern Philippines in phases 5–6 but in the north-western Philippines in phase 1. The MJO/BSISO signal in extreme precipitation frequencies was shown to be dependent on season, particularly for the northern regions of the MC, which exhibit clear wet and dry seasons, but also in eastern Sulawesi, for which both boreal winter and summer are wet seasons. These differences can be attributed to the seasonal migration of the Asian–Australian monsoon and also the fundamental difference between the MJO and the BSISO. We note that the vanguard of extreme precipitation which propagates into the equatorial regions of the MC is not a specific feature of the MJO (boreal winter) but is also present in the BSISO cycle in boreal summer.

Perhaps surprisingly, the temporal MJO cycle of extreme precipitation frequency at the mountain grid points of each region followed that of the lowland grid points fairly closely. Some caution is needed when using satellite rainfall products over mountainous regions of the MC. For example, station data from Papua New Guinea gave mean rainfall amounts and MJO rainfall anomalies with twice the values of those calculated from the satellite TRMM rainfall product over the mountains, but with very similar values over the lowland (Matthews *et al.*, 2013). Hence, the amplitude of the extreme rainfall over the mountain grid points may be underestimated. However, this would not affect the relative frequencies presented here. The MJO cycle of extreme precipitation frequency at the ocean grid points of each region also generally followed a similar pattern to their lowland and mountain equivalents.

The choice of boxes made in our study did not allow us to retrieve the vanguard of precipitation for western Sumatra and north-west Borneo in our analysis of the temporal MJO cycle of extreme precipitation frequencies. In eastern Peninsular Malaysia, however, a vanguard of extreme precipitation was identified over the land areas, ahead of the peak frequency of median precipitation in the MJO cycle. The latter vanguard of extreme precipitation is probably linked to the same physical processes as proposed by Peatman *et al.* (2014); Birch *et al.* (2016) for western Sumatra and north-western Borneo. Our study suggests that these process may occur only during the boreal winter and are associated with extreme precipitation events rather than average precipitation.

The analysis was performed using the OMI for its ability to capture the poleward propagation of the MJO/BSISO during boreal summer. The MJO RMM index (Wheeler and Hendon, 2004) is also a widely used MJO index, although less able to capture poleward propagation (Wang *et al.*, 2018). We therefore repeated the analysis replacing the OMI by the RMM index. While the main conclusions of the present study still hold when using the RMM index, results in specific areas such as those analysed in our study may differ according to the MJO index used. We therefore recommend to use the OMI for the application of our results in such localised areas.

These common results between lowland, mountain and ocean grid points within a region may be explained by the ubiquitousness of the diurnal cycle as the leading physical process governing rainfall over the MC. Rather than being washed out by any large-scale forcing, the diurnal cycle on extreme precipitation days was shown to actually increase in amplitude compared with average precipitation days. Given that the diurnal cycle within a region links

the lowland, mountain and ocean through development of convection in coastal lowland areas through sea breeze circulation through the day, with propagation inland to the mountains, and offshore over the ocean in the evening (Love *et al.*, 2011; Birch *et al.*, 2016), then the development of extreme precipitation over one surface type will then propagate across the others, leading to them all tending to show a peak in the same MJO phase. Consequently, it was found that the diurnal cycle of extreme precipitation during the MJO active phase does not differ much from the mean diurnal cycle of extreme precipitation.

Finally, an analysis of extreme rainfall through the MJO cycle was presented for the major cities or population centres in the western MC. The observed signal was strong enough to be significant (for both median and extreme rainfall) at the city scale. Hence, this observational result can provide useful guidance for forecasts based on the current and predicted state of the large-scale MJO. Additionally, with the advent of routine numerical weather prediction at convective resolving scales over large domains (Jucker *et al.*, 2020), these observational results may be used as a test-bed to assess future forecast skill.

ORCID
Nicolas A. Da Silva https://orcid.org/0000-0003-3255-9274
Adrian J. Matthews https://orcid.org/0000-0003-0492-1168

REFERENCES
Adhikari, P., Hong, Y., Douglas, K.R., Kirschbaum, D.B., Gourley, J., Adler, R. and Brakenridge, G.R. (2010) A digitized global flood inventory (1998–2008): compilation and preliminary results. *Natural Hazards*, 55, 405–422. https://doi.org/10.1007/s11069-010-9537-2.

Adler, R.F., Sapiano, M.R.P., Huffman, G.J., Wang, J.J., Gu, G., Bolvin, D., Chiu, L., Schneider, U., Becker, A., Nelkin, E., Xie, P., Ferraro, R. and Shin, D.B. (2018) The Global Precipitation Climatology Project (GPCP) monthly analysis (new version 2.3) and a review of 2017 global precipitation. *Atmosphere*, 9, 138. https://doi.org/10.3390/atmos9040138.

Alsumaiti, T.S., Hussein, K., Ghebreyesus, D.T. and Sharif, H.O. (2020) Performance of the CMORPH and GPM IMERG Products over the United Arab Emirates. *Remote Sensing*, 12, 1426. https://doi.org/10.3390/rs12091426.

As-syakur, A.R., Osawa, T., Miura, F., Nuarsa, I.W., Ekayanti, N.W., Dharma, I.G.B.S., Adnyana, I.W.S., Arthana, I.W. and Tanaka, T. (2016) Maritime continent rainfall variability during the TRMM era: the role of monsoon, topography and El Niño Modoki. *Dynamics of Atmospheres and Oceans*, 75, 58–77. https://doi.org/10.1016/j.dynatmoce.2016.05.004.

Basconcillo, J., Lucero, A., Solis, A., Sandoval, J.R., Bautista, E., Koizumi, T. and Kanamaru, H. (2016) Statistically downscaled projected changes in seasonal mean temperature and rainfall in Cagayan Valley, Philippines. *Journal of the Meteorological Society of Japan*, 94A, 151–164. https://doi.org/10.2151/jmsj.2015-058.

Birch, C.E., Webster, S., Peatman, S.C., Parker, D.J., Matthews, A.J., Li, Y. and Hassim, M.E. (2016) Scale interactions between the MJO and the western Maritime Continent. *Journal of Climate*, 29, 2471–2492. https://doi.org/10.1175/JCLI-D-15-0557.1.

Bowman, K.P. and Fowler, M.D. (2015) The diurnal cycle of precipitation in tropical cyclones. *Journal of Climate*, 28, 5325–5334. https://doi.org/10.1175/JCLI-D-14-00804.1.

Chang, C.P., Wang, Z., McBride, J. and Liu, C.H. (2005) Annual cycle of southeast Asia–Maritime Continent rainfall and the asymmetric monsoon transition. *Journal of Climate*, 18, 287–301. https://doi.org/10.1175/JCLI-3257.1.

Dewata, I. and Umar, I. (2019) Management of flood hazard areas in Pasaman River basin of West Pasaman Regency, West Sumatra Province. *International Journal GEOMATE*, 17, 230–237.

Endo, N., Matsumoto, J. and Lwin, T. (2009) Trends in precipitation extremes over Southeast Asia. *SOLA*, 5, 168–171. https://doi.org/10.2151/sola.2009-043.

Fang, J., Yang, W., Luan, Y., Du, J., Lin, A. and Zhao, L. (2019) Evaluation of the TRMM 3B42 and GPM IMERG products for extreme precipitation analysis over China. *Atmospheric Research*, 223, 24–38. https://doi.org/10.1016/j.atmosres.2019.03.001.

Gaughan, A.E., Stevens, F.R., Linard, C., Jia, P. and Tatem, A.J. (2013) High resolution population distribution maps for Southeast Asia in 2010 and 2015. *PLoS One*, 8. https://doi.org/10.1371/journal.pone.0055882. e55882.

Hall, J.D., Matthews, A.J. and Karoly, D.J. (2001) The modulation of tropical cyclone activity in the Australian region by the Madden–Julian oscillation. *Monthly Weather Review*, 129, 2970–2982. https://doi.org/10.1175/1520-0493(2001)129<2970:TMOTCA>2.0.CO;2.

Hassim, M.E.E. and Timbal, B. (2019) Observed rainfall trends over Singapore and the Maritime Continent from the perspective of regional-scale weather regimes. *Journal of Applied Meteorology and Climatology*, 58, 365–384. https://doi.org/10.1175/JAMC-D-18-0136.1.

Hijioka, Y., Lin, E., Pereira, J.J., Corlett, R.T., Cui, X., Insarov, G.E., Lasco, R.D., Lindgren, E. and Surjan, A. (2014). Asia. In V.R.

Barros, C.B. Field, D.J. Dokken, M.D. Mastrandrea, K.J. Mach, T.E. Bilir, M. Chatterjee, K.L. Ebi, Y.O. Estrada, R.C. Genova, B. Girma, E.S. Kissel, A.N. Levy, S. MacCracken, P.R. Mastrandrea, and L.L. White (Eds.), *Climate Change 2014: Impacts, Adaptation, and Vulnerability. Part B: Regional Aspects. Contribution of Working Group II to the Fifth Assessment Report of the Intergovernmental Panel on Climate Change*, pp. 1327–1370. Cambridge and New York, NY: Cambridge University Press.

Htway, O. and Matsumoto, J. (2011) Climatological onset dates of summer monsoon over Myanmar. *International Journal of Climatology*, 31, 382–393. https://doi.org/10.1002/joc.2076.

Huffman, G.J., Bolvin, D.T., Nelkin, E.J., Wolff, D.B., Adler, R.F., Gu, G., Hong, Y., Bowman, K.P. and Stocker, E.F. (2007) The TRMM Multisatellite Precipitation Analysis (TMPA): quasi-global, multiyear, combined-sensor precipitation estimates at fine scales. *Journal of Hydrometeorology*, 8, 38–55. https://doi.org/10.1175/JHM560.1.

Huffman, G.J., Stocker, E.F., Bolvin, D.T., Nelkin, E.J. and Tan, J. (2019). GPM IMERG final precipitation L3 half hourly 0.1 degree x 0.1 degree V06, Greenbelt, MD, Goddard Earth Sciences Data and Information Services Center (GES DISC, last access: 5 June 2020).

Jamaluddin, A.F., Tangang, F., Chung, J.X., Juneng, L., Sasaki, H. and Takayabu, I. (2018) Investigating the mechanisms of diurnal rainfall variability over Peninsular Malaysia using the non-hydrostatic regional climate model. *Meteorology and Atmospheric Physics*, 130, 611–633. https://doi.org/10.1007/s00703-017-0541-x.

Jiang, X., Li, T. and Wang, B. (2004) Structures and mechanisms of the northward propagating boreal summer intraseasonal oscillation. *Journal of Climate*, 17, 1022–1039. https://doi.org/10.1175/1520-0442(2004)017<1022:SAMOTN>2.0.CO;2.

Joyce, R.J., Janowiak, J.E., Arkin, P.A. and Xie, P. (2004) CMORPH: a method that produces global precipitation estimates from passive microwave and infrared data at high spatial and temporal resolution. *Journal of Hydrometeorology*, 5, 487–503. https://doi.org/10.1175/1525-7541(2004)005<0487:CAMTPG>2.0.CO;2.

Joyce, R.J. and Xie, P. (2011) Kalman filter–based CMORPH. *Journal of Hydrometeorology*, 12, 1547–1563. https://doi.org/10.1175/JHM-D-11-022.1.

Jucker, M., Lane, T.P., Vincent, C.L., Webster, S., Wales, S.A. and Louf, V. (2020) Locally forced convection in sub-kilometre scale simulations with the Unified Model and WRF. *Quarterly Journal of the Royal Meteorological Society*. https://doi.org/10.1002/qj.3855. published online.

Juneng, L. and Tangang, F.T. (2005) Evolution of ENSO-related rainfall anomalies in southeast Asia region and its relationship with atmosphere–ocean variations in Indo-Pacific sector. *Climate Dynamics*, 25, 337–350. https://doi.org/10.1007/s00382-005-0031-6.

Kang, S., Im, E.S. and Eltahir, E.A.B. (2019) Future climate change enhances rainfall seasonality in a regional model of western Maritime Continent. *Climate Dynamics*, 52, 747–764. https://doi.org/10.1007/s00382-018-4164-9.

Kiladis, G.N., Dias, J., Straub, K.H., Wheeler, M.C., Tulich, S.N., Kikuchi, K., Weickmann, K.M. and Ventrice, M.J. (2014) A comparison of OLR and circulation-based indices for tracking the MJO. *Monthly Weather Review*, 142, 1697–1715. https://doi.org/10.1175/MWR-D-13-00301.1.

Kim, K., Park, J., Baik, J. and Choi, M. (2017) Evaluation of topographical and seasonal feature using GPM IMERG and TRMM 3B42 over far-east Asia. *Atmospheric Research*, 187, 95–105. https://doi.org/10.1016/j.atmosres.2016.12.007.

Kim, D., Kim, H. and Lee, M.I. (2017) Why does the MJO detour the Maritime Continent during austral summer?. *Geophysical Research Letters*, 44, 579–2587. https://doi.org/10.1002/2017GL072643.

Kim, H., Vitart, F. and Waliser, D.E. (2018) Prediction of the Madden–Julian oscillation: a review. *Journal of Climate*, 31, 9425–9443. https://doi.org/10.1175/JCLI-D-18-0210.1.

Krishnamurti, T.N. and Subrahmanyam, D. (1982) The 30–50 Day Mode at 850 mb During MONEX. *Journal of the Atmospheric Sciences*, 39, 2088–2095. https://doi.org/10.1175/1520-0469(1982)039<2088:TDMAMD>2.0.CO;2.

Kummerow, C., Simpson, J., Thiele, O., Barnes, W., Chang, A.T.C., Stocker, E., Adler, R.F., Hou, A., Kakar, R., Wentz, P., Ashcroft, F., Kozu, T., Hong, Y., Okamoto, K., Iguchi, T., Kuroiwa, H., Im, E., Haddad, Z., Huffman, G., Ferrier, B., Olson, W.S., Zipser, E., Smith, E.A., Wilheit, T.T., North, G., Krishnamurti, T. and Nakamura, K. (2000) The status of the Tropical Rainfall Measuring Mission (TRMM) after two years in orbit. *Journal of Applied Meteorology*, 39, 1965–1982. https://doi.org/10.1175/1520-0450(2001)040<1965:TSOTTR>2.0.CO;2.

Lee, J., Lee, E.H. and Seol, K.H. (2019) Validation of Integrated MultisatellitE Retrievals for GPM (IMERG) by using gauge-based analysis products of daily precipitation over East Asia. *Theoretical and Applied Climatology*, 137, 2497–2512. https://doi.org/10.1007/s00704-018-2749-1.

Love, B.S., Matthews, A.J. and Lister, G.M.S. (2011) The diurnal cycle of precipitation over the Maritime Continent in a high-resolution atmospheric model. *Quarterly Journal of the Royal Meteorological Society*, 137, 934–947. https://doi.org/10.1002/qj.809.

Madden, R.A. and Julian, P.R. (1971) Detection of a 40–50 day oscillation in the zonal wind in the tropical Pacific. *Journal of the Atmospheric Sciences*, 28, 702–708. https://doi.org/10.1175/1520-0469(1971)028<0702:DOADOI>2.0.CO;2.

Mandapaka, P.V. and Lo, E.Y.M. (2018) Assessment of future changes in southeast Asian precipitation using the NASA Earth Exchange Global Daily Downscaled Projections data set. *International Journal of Climatology*, 38, 5231–5244. https://doi.org/10.1002/joc.5724.

Mandapaka, P.V. and Lo, E.Y.M. (2020) Evaluation of GPM IMERG rainfall estimates in Singapore and assessing spatial sampling errors in ground reference. *Journal of Hydrometeorology*, 21, 2963–2977. https://doi.org/10.1175/JHM-D-20-0135.s1.

Matthews, A.J., Pickup, G., Peatman, S.C., Clews, P. and Martin, J. (2013) The effect of the Madden–Julian Oscillation on station rainfall and river level in the Fly River system, Papua New Guinea. *Journal of Geophysical Research*, 118, 10926–10935. https://doi.org/10.1002/jgrd.50865.

Meehl, G.A. (1987) The annual cycle and interannual variability in the tropical Pacific and Indian Ocean regions. *Monthly Weather Review*, 115, 27–50. https://doi.org/10.1175/1520-0493(1987)115<0027:TACAIV>2.0.CO;2.

Nguyen, P., Ombadi, M., Sorooshian, S., Hsu, K., AghaKouchak, A., Braithwaite, D., Ashouri, H. and Thorstensen, A.R. (2018) The PERSIANN family of global satellite precipitation data: a review and evaluation of products. *Hydrology and Earth System*

Sciences, 22, 5801–5816. https://doi.org/10.5194/hess-22-5801-2018.

Oh, J.H., Kwang-Yul, K. and Gyu-Ho, L. (2012) Impact of MJO on the diurnal cycle of rainfall over the western Maritime Continent in the austral summer. *Climate Dynamics*, 38, 1167–1180. https://doi.org/10.1007/s00382-011-1237-4.

Peatman, S.C., Matthews, A.J. and Stevens, D.P. (2014) Propagation of the Madden–Julian oscillation through the Maritime Continent and scale interaction with the diurnal cycle of precipitation. *Quarterly Journal of the Royal Meteorological Society*, 140, 814–825. https://doi.org/10.1002/qj.2161.

Prakash, S., Mitra, A.K., Pai, D.S. and AghaKouchak, A. (2016) From TRMM to GPM: how well can heavy rainfall be detected from space?. *Advances in Water Resources*, 88, 1–7. https://doi.org/10.1016/j.advwatres.2015.11.008.

Prat, O.P. and Nelson, B.R. (2013) Mapping the world's tropical cyclone rainfall contribution over land using the TRMM Multi-satellite Precipitation Analysis. *Water Resources Research*, 49, 7236–7254. https://doi.org/10.1002/wrcr.20527.

Qian, J.H. (2008) Why precipitation is mostly concentrated over islands in the Maritime Continent. *Journal of the Atmospheric Sciences*, 65, 1428–1441. https://doi.org/10.1175/2007JAS2422.1.

Rodysill, J.R., Russell, J.M., Vuille, M., Dee, S., Lunghino, B. and Bijaksana, S. (2019) La Niña-driven flooding in the Indo–Pacific warm pool during the past millenium. *Quaternary Science Reviews*, 225, 106020. https://doi.org/10.1016/j.quascirev.2019.106020.

Skofronick-Jackson, G., Kirschbaum, D., Petersen, W., Huffman, G., Kidd, C., Stocker, E. and Kakar, R. (2018) The Global Precipitation Measurement (GPM) mission's scientific achievements and societal contributions: reviewing four years of advanced rain and snow observations. *Quarterly Journal of the Royal Meteorological Society*, 144, 27–48. https://doi.org/10.1002/qj.3313.

Tan, M.L. and Santo, H. (2018) Comparison of GPM IMERG, TMPA 3B42 and PERSIANN-CDR satellite precipitation products over Malaysia. *Atmospheric Research*, 202, 63–76. https://doi.org/10.1016/j.atmosres.2017.11.006.

Tangang, F., Farzanmanesh, R., Mirzaei, A., Supari, S.E., Jamaluddin, A.F. and Juneng, L. (2017) Characteristics of precipitation extremes in Malaysia associated with El Niño and La Niña events. *International Journal of Climatology*, 37, 696–716. https://doi.org/10.1002/joc.5032.

Wang, S. and Sobel, A.H. (2017) Factors controlling rain on small tropical islands: diurnal cycle, large-scale wind speed, and topography. *Journal of the Atmospheric Sciences*, 74, 3515–3532. https://doi.org/10.1175/JAS-D-16-0344.1.

Wang, S., Ma, D., Sobel, A.H. and Tippett, M.K. (2018) Propagation characteristics of BSISO indices. *Geophysical Research Letters*, 45, 9934–9943. https://doi.org/10.1029/2018GL078321.

Wang, S., Sobel, A.H., Tippett, M.K. and Vitart, F. (2019) Prediction and predictability of tropical intraseasonal convection: seasonal dependence and the Maritime Continent prediction barrier. *Climate Dynamics*, 52, 6015–6031. https://doi.org/10.1007/s00382-018-4492-9.

Wei, G., Lü, H., Crow, W.T., Zhu, Y., Wang, J. and Su, J. (2018) Comprehensive evaluation of GPM IMERG, CMORPH, and TMPA precipitation products with gauged rainfall over mainland China. *Advances in Meteorology*, 2018, 3024190. https://doi.org/10.1155/2018/3024190.

Wheeler, M.C. and Hendon, H.H. (2004) An all-season real-time multi-variate MJO index: development of an index for monitoring and prediction. *Monthly Weather Review*, 132, 1917–1932. https://doi.org/10.1175/1520-0493(2004)132<1917:AARMMI>2.0.CO;2.

Xavier, P., Rahmat, R., Cheong, W.K. and Wallace, E. (2014) Influence of Madden–Julian oscillation on Southeast Asia rainfall extremes: observations and predictability. *Geophysical Research Letters*, 41, 4406–4412. https://doi.org/10.1002/2014GL060241.

Xiao, S., Xia, J. and Zou, L. (2020) Evaluation of multi-satellite precipitation products and their ability in capturing the characteristics of extreme climate events over the Yangtze River Basin, China. *Water*, 12, 1179. https://doi.org/10.3390/w12041179.

Xie, Y.B., Chen, S.J., Zhang, I.L. and Hung, Y.L. (1963) A preliminarily statistic and synoptic study about the basic currents over southeastern Asia and the initiation of typhoon (in Chinese). *Acta Meteorologica Sinica*, 33, 206–217.

Xu, F., Guo, B., Ye, B., Ye, Q., Chen, H., Ju, X., Guo, J. and Wang, Z. (2019) Systematical evaluation of GPM IMERG and TRMM 3B42V7 precipitation products in the Huang-Huai-Hai Plain, China. *Remote Sensing*, 11, 697. https://doi.org/10.3390/rs11060697.

Yang, G.Y. and Slingo, J.M. (2001) The diurnal cycle in the Tropics. *Monthly Weather Review*, 129, 784–801. https://doi.org/10.1175/1520-0493(2001)129<0784:TDCITT>2.0.CO;2.

Yasunari, T. (1979) Cloudiness Fluctuations Associated with the Northern Hemisphere Summer Monsoon. *Journal of the Meteorological Society of Japan*, 57, 227–242. https://doi.org/10.2151/jmsj1965.57.3_227.

Yatagai, A., Kamiguchi, K., Arakawa, O., Hamada, A., Yasutomi, N. and Kitoh, A. (2012) APHRODITE: constructing a long-term daily gridded precipitation dataset for Asia based on a dense network of rain gauges. *Bulletin of the American Meteorological Society*, 93, 1401–1415. https://doi.org/10.1175/BAMS-D-11-00122.1.

Zhang, C. and Dong, M. (2004) Seasonality in the Madden—Julian Oscillation. *Journal of Climate*, 17, 3169–3180. https://doi.org/10.1175/1520-0442(2004)017<3169:SITMO>2.0.CO;2.

Zhang, T., Yang, S., Jiang, X. and Zhao, P. (2016) Seasonal–interannual variation and prediction of wet and dry season rainfall over the Maritime Continent: roles of ENSO and monsoon circulation. *Journal of Climate*, 29, 3675–3695. https://doi.org/10.1175/JCLI-D-15-0222.1.

Zhu, L., Chen, X. and Bai, L. (2020) Relative roles of low-level wind speed and moisture in the diurnal cycle of rainfall over a Tropical Island under monsoonal flows. *Geophysical Research Letters*, 47. e2020GL087467. https://doi.org/10.1029/2020GL087467.